The complete structure of the human TFIIH core complex

Basil J. Greber[1,2], Daniel B. Toso[1], Jie Fang[3], Eva Nogales[1,2,3,4,*]

[1] California Institute for Quantitative Biosciences (QB3), University of California, Berkeley, California 94720, USA

[2] Molecular Biophysics and Integrative Bio-Imaging Division, Lawrence Berkeley National Laboratory, Berkeley, California 94720, USA

[3] Howard Hughes Medical Institute, University of California, Berkeley, California 94720, USA

[4] Department of Molecular and Cell Biology, University of California, Berkeley, California 94720, USA

[*] **For correspondence:** Enogales@lbl.gov (E.N.)

Competing interests: The authors declare that no competing interests exist.

ABSTRACT

Transcription factor IIH (TFIIH) is a heterodecameric protein complex critical for transcription initiation by RNA polymerase II and nucleotide excision DNA repair. The TFIIH core complex is sufficient for its repair functions and harbors the XPB and XPD DNA-dependent ATPase/helicase subunits, which are affected by human disease mutations. Transcription initiation additionally requires the CdK activating kinase subcomplex. Previous structural work has provided only partial insight into the architecture of TFIIH and its interactions within transcription pre-initiation complexes. Here, we present the complete structure of the human TFIIH core complex, determined by phase-plate cryo-electron microscopy at 3.7 Å resolution. The structure uncovers the molecular basis of TFIIH assembly, revealing how the recruitment of XPB by p52 depends on a pseudo-symmetric dimer of homologous domains in these two proteins. The structure also suggests a function for p62 in the regulation of XPD, and allows the mapping of previously unresolved human disease mutations.

INTRODUCTION

Transcription factor IIH (TFIIH) is a 10-subunit protein complex with a total molecular weight of 0.5 MDa that serves a dual role as a general transcription factor for transcription initiation by eukaryotic RNA polymerase II (Pol II), and as a DNA helicase complex in nucleotide excision DNA repair (NER) (Compe & Egly, 2016; Sainsbury et al., 2015). Mutations in TFIIH subunits that cause the inherited autosomal recessive disorders xeroderma pigmentosum (XP), trichothiodystrophy (TTD), and Cockayne syndrome (CS) are characterized by high incidence of cancer or premature ageing (Cleaver et al., 1999; Rapin, 2013). Furthermore, TFIIH is a possible target for anti-cancer compounds (Berico & Coin, 2017) and therefore of great importance for human health and disease.

The TFIIH core complex is composed of the seven subunits XPB, XPD, p62, p52, p44, p34, and p8, and is the form of TFIIH active in DNA repair (Svejstrup et al., 1995), where TFIIH serves as a DNA damage verification factor (Li et al., 2015;

52 Mathieu et al., 2013) and is responsible for opening a repair bubble around
53 damaged nucleotides. This activity depends on both the SF2-family DNA-
54 dependent ATPase XPB, and the DNA helicase activity of XPD (Coin et al., 2007;
55 Evans et al., 1997; Kuper et al., 2014). TFIIH function in transcription initiation
56 requires the double-stranded DNA translocase activity of XPB to regulate
57 opening of the transcription bubble (Alekseev et al., 2017; Fishburn et al., 2015;
58 Grünberg et al., 2012), and additionally the CdK activating kinase (CAK) complex,
59 which harbors the kinase activity of CDK7 as well as the Cyclin H and MAT1
60 subunits (Devault et al., 1995; Fisher et al., 1995; Fisher & Morgan, 1994;
61 Shiekhattar et al., 1995; Svejstrup et al., 1995). Targets of human CDK7 include
62 the C-terminal heptapeptide repeat domain of the largest subunit of Pol II, as
63 well as cell-cycle regulating CDKs (Fisher & Morgan, 1994; Shiekhattar et al.,
64 1995). MAT1 serves as a bridging subunit that promotes CAK subcomplex
65 formation by interacting with Cyclin H and CDK7 (Devault et al., 1995; Fisher et
66 al., 1995), recruits the CAK to the core complex by interactions with XPD and XPB
67 (Abdulrahman et al., 2013; Busso et al., 2000; Greber et al., 2017; Rossignol et al.,
68 1997), and also aids in Pol II-PIC formation by establishing interactions with the
69 core PIC (He et al., 2013; He et al., 2016; Schilbach et al., 2017). The presence of
70 MAT1 inhibits the helicase activity of XPD (Abdulrahman et al., 2013; Sandrock &
71 Egly, 2001), but the mechanism of this inhibition is not fully understood. While
72 the enzymatic activity of XPD is not required for transcription initiation, it is
73 critical for the DNA repair function of TFIIH (Dubaele et al., 2003; Evans et al.,
74 1997; Kuper et al., 2014). Therefore, NER requires the release of the CAK
75 subcomplex from the core complex (Coin et al., 2008). The activities of both XPB
76 and XPD are regulated by interactions with additional TFIIH components,
77 including that of p44 with XPD (Coin et al., 1998; Dubaele et al., 2003; Kim et al.,
78 2015), and those of the p52-p8 module with XPB (Coin et al., 2007; Coin et al.,
79 2006; Jawhari et al., 2002; Kainov et al., 2008). These interactions are likely to be
80 crucial for TFIIH function, as some are affected by disease mutations (Cleaver et
81 al., 1999), but they have been only partially characterized mechanistically.
82
83 Our previous structure of the TFIIH core-MAT1 complex at 4.4 Å resolution
84 (Greber et al., 2017) allowed modeling of TFIIH in the best-resolved parts of the

density map, but several functionally important regions remained unassigned or only partially interpreted because reliable *de novo* tracing of entire domains in the absence of existing structural models was not possible. Here, we present the complete structure of the human TFIIH core complex in association with the CAK subunit MAT1, determined by phase plate cryo-electron microscopy (cryo-EM) at 3.7 Å resolution. Our structure reveals the complete architecture of the TFIIH core complex and provides detailed insight into the interactions that govern its assembly. Additionally, our cryo-EM maps define the molecular contacts that control the regulation of the XPB and XPD subunits of TFIIH, including the critical p52-XBP interaction, and an extensive regulatory network around XPD, formed by XPB, p62, p44, and MAT1.

RESULTS

Structure determination of TFIIH

To determine the complete structure of the human TFIIH core complex, we collected several large cryo-EM datasets (Supplementary Table 1) of TFIIH immuno-purified from HeLa cells using an electron microscope equipped with a Volta phase plate (VPP) (Danev & Baumeister, 2017) and a direct electron detector camera mounted behind an energy filter. From a homogeneous subset of approximately 140,000 TFIIH particle images identified by 3D classification (Scheres, 2010), we reconstructed a 3D cryo-EM density map at 3.7 Å resolution (Figure 1 – figure supplements 1, 2A-C). This VPP-based cryo-EM map was substantially improved compared to our previous maps obtained without phase plate, both in resolution and interpretability (Figure 1 – figure supplement 2D-G), and enabled building, refinement, and full validation of an atomic model of the TFIIH core complex and the MAT1 subunit of the CAK subcomplex (Figure 1A-C, Figure 1 – figure supplement 2B, C, Supplementary Tables 2, 3), while the remainder of the CAK is invisible in our map due to extreme motion. Tracing and sequence register assignment of protein components modeled *de novo* was facilitated by density maps obtained from focused classification and multibody refinement (Figure 1 – figure supplements 3-5) (Bai et al., 2015; Nakane et al.,

2018), which resulted in density maps for sub-volumes of the complex at up to 3.6 Å resolution. Both the overall and multibody-refined maps showed clear side chain information (Figure 1 – figure supplement 6A-D). Furthermore, our model was corroborated by existing chemical crosslinking-mass spectrometry (CX-MS) data of human TFIIH (Luo et al., 2015) and site-specific crosslinks from yeast TFIIH (Warfield et al., 2016) (Figure 1 – figure supplement 6E-I).

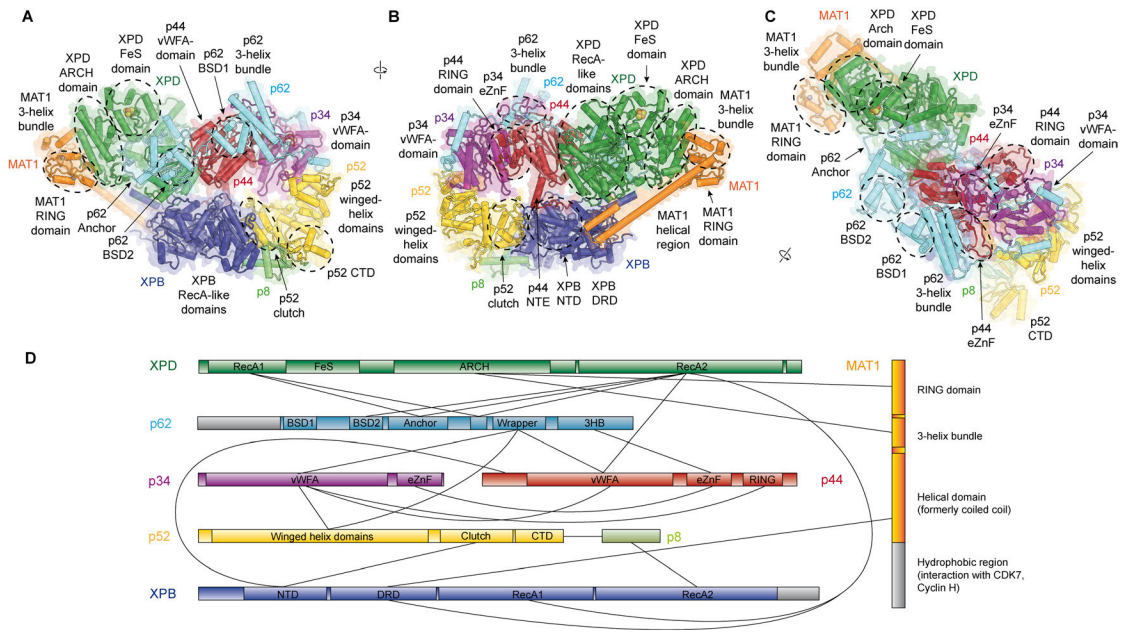

Figure 1. Structure of the TFIIH core complex. (**A**, **B**, **C**) Three views of the structure of the TFIIH core complex and MAT1. Subunits are color-coded and labeled (in color); individual domains are labeled (in black) and circled if needed for clarity. (**D**) Domain-level interaction network between the components of the TFIIH core complex and MAT1 derived from our structure. Proteins are shown with the same colors as in A and major unmodeled regions are shown in grey. Abbreviations: CTD: C-terminal domain; DRD: DNA damage recognition domain; FeS: iron sulfur cluster domain; NTD: N-terminal domain; vWFA: von Willebrand Factor A.

Figure supplement 1. Data processing scheme for global reconstruction.

Figure supplement 2. Resolution estimation, validation statistics, and quality of the density.

Figure supplement 3. Focused classification of the p62 BSD2 domain.

140 **Figure supplement 4.** Focused classification and interpretation of the MAT1
141 RING domain density.
142 **Figure supplement 5.** Multibody refinement.
143 **Figure supplement 6.** Detailed architecture of the TFIIH core complex.
144
145 **Detailed architecture of TFIIH and structure of p62**
146
147 Our structure of the TFIIH core complex shows its horseshoe-like overall shape
148 (Figure 1A-C), as observed in previous lower-resolution reconstructions of free
149 and PIC-bound TFIIH (Gibbons et al., 2012; Greber et al., 2017; He et al., 2016;
150 Murakami et al., 2015; Schilbach et al., 2017), and allows us to define the
151 complete set of inter-subunit interactions that lead to the formation of the TFIIH
152 core complex (Figure 1D).
153
154 The largest subunits of the complex, the SF2-family DNA-dependent ATPases
155 XPB and XPD, both containing two RecA-like domains (RecA1 and RecA2),
156 interact directly (Greber et al., 2017) and are on one side of the complex, and are
157 additionally bridged by MAT1 (Figure 1B), which has been shown to interact
158 with either ATPase in isolation (Busso et al., 2000). On the side facing away from
159 MAT1, XPD interacts with the von Willebrand Factor A (vWFA) domain of p44
160 (Coin et al., 1998; Dubaele et al., 2003; He et al., 2016; Kim et al., 2015), which in
161 turn forms a tight interaction with p34 via interlocking eZnF domains (Schilbach
162 et al., 2017) and a p44 RING domain interaction (Radu et al., 2017) (Figure 1B-D,
163 Figure 1 – figure supplement 6J, K), consistent with the formation of a
164 multivalent interaction network between p34 and p44 (Radu et al., 2017). The
165 vWFA domain of p34 recruits p52 by a three-way interaction that involves the
166 most N-terminal winged helix domain in p52 and a helical segment of p62
167 (Schilbach et al., 2017) (Figure 1 – figure supplement 6L). The p52 C-terminal
168 region comprises two domains; first, the 'clutch' that interacts with XPB (Jawhari
169 et al., 2002) and second, a dimerization module that binds p8 (Kainov et al.,
170 2008), thereby recruiting XPB to TFIIH and cradling XPB RecA2 (see below). In
171 addition to this structural framework that is formed by folded domains, our cryo-
172 EM map reveals several interactions involving extended protein segments,

173 including several interactions formed by p62 (Figure 2), and an interaction
174 between the p44 N-terminal extension (NTE) and the N-terminal domain (NTD)
175 of XPB (Figure 1B). To form this interaction, approx. 15 residues of p44 span the
176 distance between the p44 vWFA domain and the XPB NTD, where a small helical
177 motif in p44 contacts XPB residues 72-75, 95-102, and 139-143, in agreement
178 with CX-MS data (Luo et al., 2015) (Figure 1 – figure supplement 6E). Partial
179 deletion of the p44 NTE in yeast causes a slow-growth phenotype, suggesting a
180 functional role for this p44-XPB interaction (Warfield et al., 2016).
181

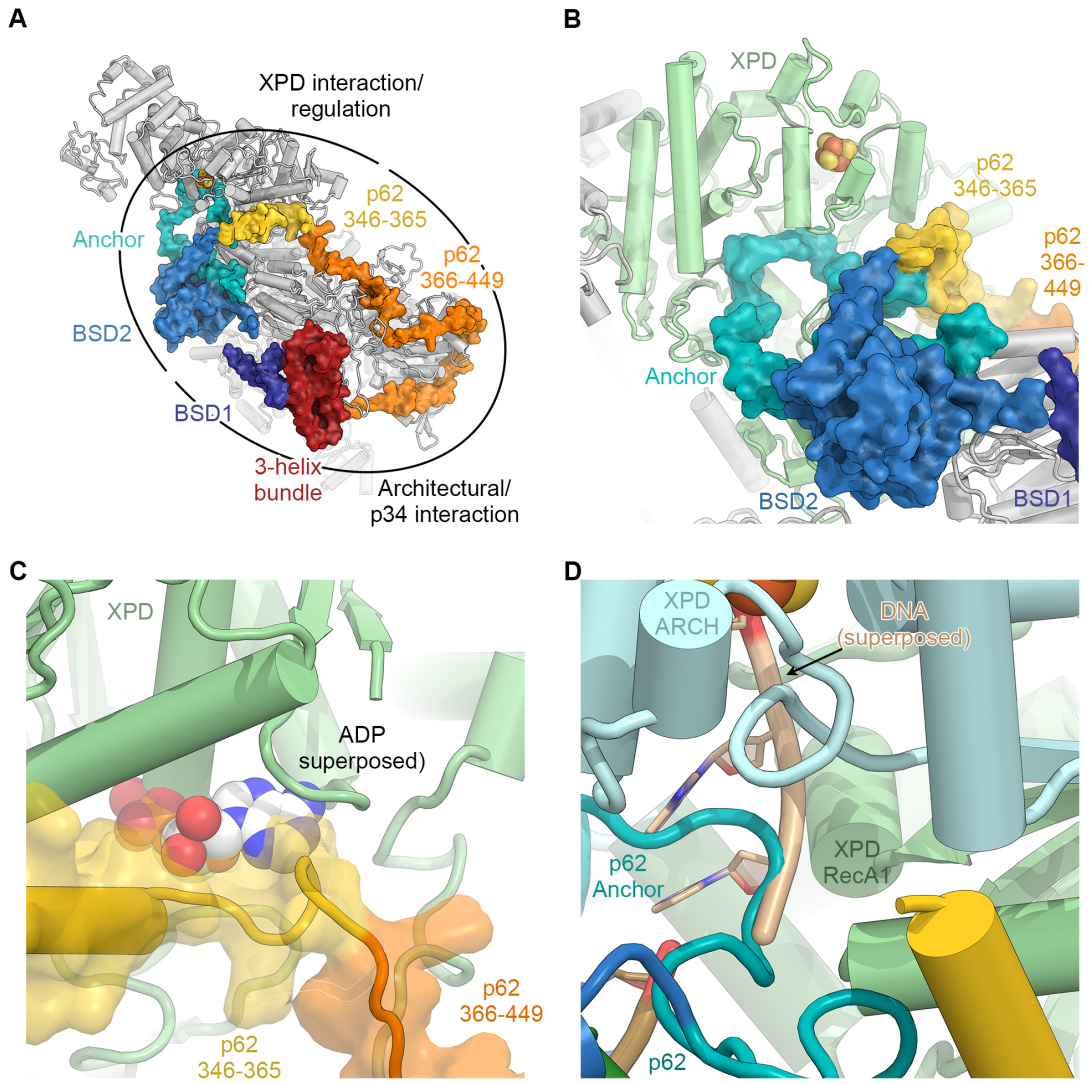

182
183 **Figure 2. The structure of p62.** (**A**) View of the top surface of the TFIIH core
184 complex; p62 is color-coded by structural region. (**B**) The BSD2 (blue) and XPD
185 anchor segments (teal) of p62 (surface) interact with the region around the XPD
186 substrate-binding cavity. (**C**) Residues 346-365 of p62 (yellow) approach the

187 nucleotide-binding pocket of XPD. ADP superposed from the structure of the
188 Brr2 helicase (Nguyen et al., 2013). (**D**) Superposition of DNA from the structure
189 of the substrate-bound helicase Hel308 (Büttner et al., 2007) shows that the
190 positions of p62 and RecA1-bound DNA overlap.
191
192 **Figure supplement 1.** Analysis of the structure of p62.
193
194 The p62 subunit is almost completely resolved in our structure and exhibits a
195 complex beads-on-a-string-like topology. It fully encircles the top surface of
196 TFIIH (Figures 1C, 2A, Figure 2 – figure supplement 1), interacting with XPD,
197 p52, p44, and p34, in agreement with previous structural findings (Greber et al.,
198 2017; Schilbach et al., 2017). Based on these interactions, p62 can be subdivided
199 into three functional regions: (i) the N-terminal PH-domain, disordered in our
200 structure, is responsible for mediating interactions with components of the core
201 transcriptional machinery (Di Lello et al., 2008; He et al., 2016; Schilbach et al.,
202 2017), transcriptional regulators (Di Lello et al., 2006), and DNA repair pathways
203 (Gervais et al., 2004; Lafrance-Vanasse et al., 2013; Okuda et al., 2017); (ii)
204 residues 108-148 and 454-548 of p62, including the first BSD (BTF2-like,
205 synapse-associated, DOS2-like) domain (BSD1) and the C-terminal 3-helix
206 bundle, play an architectural role by binding to p34 and the extended zinc finger
207 (eZnF) domain of p44 (Figure 2A, C, Figure 1 – figure supplement 6J-L, Figure 2 –
208 figure supplement 1B, C); and (iii) residues 160-365, including the BSD2 domain,
209 are responsible for interactions with and regulation of XPD (Figure 2B-D, Figure
210 2 – figure supplement 1D-F).
211
212 Specifically, p62 residues 160-365 form three structural elements that interact
213 with XPD (Figure 2B), in agreement with previous biochemical, structural, and
214 CX-MS data (Figure 1 – figure supplement 6G) (Jawhari et al., 2004; Luo et al.,
215 2015; Schilbach et al., 2017). First, an α-helix formed by p62 residues 295-318
216 binds directly to XPD RecA2 and thereby recruits residues 160-258 of p62,
217 comprising the BSD2 domain and adjacent sequence elements, to this surface of
218 XPD RecA2 (Figures 2A, B, Figure 2 – figure supplement 1D). Second, p62
219 residues 266-287 are inserted into the DNA-binding cavity of XPD (Figures 2B,

220 D), in agreement with previous observations (Schilbach et al., 2017). This
221 inserted p62 segment directly blocks a DNA-binding site on XPD RecA1 (Figure
222 2D) and localizes near the access path to a pore-like structure between the XPD
223 FeS and ARCH domains. While p62 does not directly contact the DNA-binding
224 surface on XPD RecA2, it may still sterically interfere with DNA binding to the
225 helicase elements of XPD in this region (Figure 2 – figure supplement 1E).
226 Therefore, this segment of p62 may need to move away when XPD binds and
227 unwinds DNA. Third, p62 residues 350-358 form a short α-helix that binds in a
228 cleft between the two RecA-like domains of XPD (Figure 2C), so that it not only
229 closes the entrance to the nucleotide binding pocket in XPD RecA1 (Figure 2 –
230 figure supplement 1F), but also partially overlaps with the predicted location of
231 the nucleotide itself (Figure 2C), strongly suggesting a role for this p62 sequence
232 element in XPD regulation. The density for these structural elements of p62
233 (residues 260-300 and 346-365) in our cryo-EM map is weaker than for the
234 remainder of the complex, suggesting a dynamic interaction with XPD that
235 enables them to modulate the access to the nucleotide-binding pocket, the DNA-
236 binding cavity, and the DNA-translocating pore of XPD, depending on the
237 functional state of TFIIH. 3D reconstructions of TFIIH classified for these regions
238 of p62 (Figure 1 – figure supplement 3) show globally intact TFIIH, both in the
239 presence and absence of the p62 segments at these XPD sites (Figure 2 – figure
240 supplement 1G-J), supporting our hypothesis of dynamic regulation, rather than
241 the alternative hypothesis of p62 binding to XPD as a requirement for TFIIH
242 stability (Luo et al., 2015).
243
244 **Molecular basis of XPB recruitment by p52**
245
246 Our structure of TFIIH resolves the structure and interactions of all four folded
247 domains of human XPB – two RecA-like domains that form the SF2-family type
248 helicase cassette, a DNA damage recognition domain (DRD)-like domain, and an
249 N-terminal domain (NTD) (Figure 3A, Figure 3 – figure supplement 1) – and
250 reveals the molecular basis of XPB recruitment by p52. The XPB NTD
251 encompasses residues 1-165, with the first 55 residues forming an N-terminal
252 extension (NTE), and the remainder assuming a mixed α/β-fold with four α-

253 helices and five β-strands (Figure 3A). The side chain densities in the cryo-EM
254 map (Figure 1 – figure supplement 6A) and CX-MS data (Luo et al., 2015) (Figure
255 1 – figure supplement 6F) both confirm our assignment of this domain. Existing
256 biochemical data show that the XPB NTD is required for integration of XPB into
257 TFIIH (Jawhari et al., 2002) by forming an interaction with p52 that has been
258 referred to as the 'clutch' (Schilbach et al., 2017). In our structure, the p52
259 contribution to the clutch encompasses p52 residues 306-399, which, strikingly,
260 assume the same overall fold as the XPD NTD (Figure 3B), as hypothesized
261 previously (He et al., 2016; Luo et al., 2015), thereby forming a pseudo-
262 symmetric dimer of structurally homologous domains. The two domains interact
263 through their β-sheets, via both hydrophobic and charged interactions (Figure 3
264 – figure supplement 2A-C), and with the most N-terminal β-strand emanating
265 from the XPB NTD extending the p52 β-sheet by additional lateral interactions
266 (Figure 3A, C).
267
268 Our structural findings rationalize biochemical data that show that deletion of
269 XPB residues 1-207, but not deletion of residues 1-44, impairs the p52-XPB
270 interaction (Jawhari et al., 2002) (Figure 3C). Our structure is also consistent
271 with data indicating that p52 residues 304-381 are critical for the XPB-p52
272 interaction (Coin et al., 2007; Jawhari et al., 2002), but does not show any
273 contacts that could explain that reported binding of XPB to p52 residues 1-135
274 or 1-304 (Jawhari et al., 2002) (Figure 3 – figure supplement 2D, E). The
275 interaction between p52 and XPB not only recruits XPB to TFIIH, but also
276 stimulates its ATPase activity *in vitro* (Coin et al., 2007). Because our structure
277 does not shown any elements of p52 approaching the XPB nucleotide-binding
278 pocket, we propose that this effect is likely induced by the interactions of p52
279 with the XPB NTD and RecA2, which may, together with p8 (Coin et al., 2006),
280 properly arrange the XPB helicase cassette to bind and hydrolyze ATP (Figure
281 3D) (Grünberg et al., 2012).

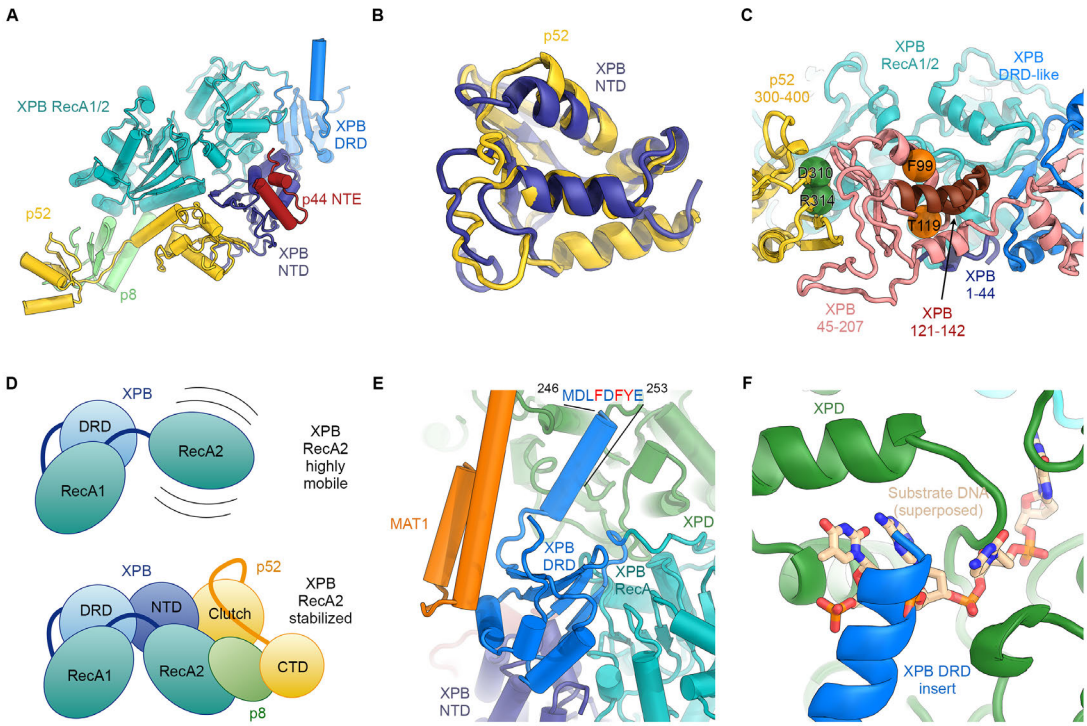

Figure 3. Structure and interactions of XPB. (**A**) Bottom lobe of TFIIH. XPB RecA1/2 teal, DRD blue, NTD dark blue, p52 yellow, p8 green, p44 NTE red. (**B**) Superposition of the XPB NTD and the p52 clutch domain. (**C**) Mapping of mutations on the XPB NTD and the p52 clutch domain; mutated regions are color-coded or shown as spheres (see text for details). (**D**) The combined interactions of the p52 clutch, the p8-p52 CTD dimer, and the XPB NTD with XPB RecA2 may restrict the conformational flexibility of XPB RecA2 to optimize XPB activity. (**E**) An extension of the DRD (blue) contacts XPD (green). The sequence for which formation of an α-helix is predicted (Kelley et al., 2015) is indicated. (**F**) The DRD extension overlaps with the substrate-binding site on XPD RecA2. Substrate DNA modeled from PDB ID 5HW8 (Constantinescu-Aruxandei et al., 2016).

Figure supplement 1. Domain organization of XPB and sequence alignment of the N-terminal regions of XPB and XPB-like enzymes from eukaryotes, archaea, and bacteria.

Figure supplement 2. Structure and interactions of the XPB DRD and NTD.

302 The XPB NTD is the site of the two human disease mutations F99S and T119P,
303 which cause XP and TTD, respectively (Cleaver et al., 1999). Or structure shows
304 that neither of these residues is in direct contact with p52 or the RecA-like
305 domains of XPB, suggesting that the F99S and T119P mutations exert their
306 detrimental effects through structural perturbation of the XPB NTD (Figure 3 –
307 figure supplements 1B, 2F-I). Specifically, T119 is located near a turn at the end
308 of a β-strand (Figure 3 – figure supplement 2G), where its side chain points
309 towards the solvent. Nevertheless, this residue is highly conserved in eukaryotic
310 XPB from ciliates to humans, in some archaeal and bacterial XPB homologs
311 (Figure 3 – figure supplement 1B), and in the structurally homologous clutch
312 domain in p52 (Figure 3 – figure supplement 2F-H). This conservation suggests
313 that a threonine at this position is important for the efficient folding of this
314 domain in general, and that the T119P mutation may cause its destabilization,
315 resulting in lower levels of active enzyme in TTD patients. Lower overall levels of
316 properly assembled TFIIH have been shown to be a hallmark of TTD (Botta et al.,
317 2002; Dubaele et al., 2003; Giglia-Mari et al., 2004) and could explain the disease-
318 causing effect of T119P *in vivo* even though recombinant TFIIH carrying this
319 mutation retains some activity in both transcription initiation and NER (Coin et
320 al., 2007). A less likely alternative, given the conservation of the equivalent
321 residue in the p52 clutch, is that T119 is involved in an interaction with a factor
322 that is critical for cellular function, e.g. in NER.
323
324 The F99S mutation affects a residue that is conserved throughout eukaryotic XPB
325 (Figure 3 – figure supplement 1B), is inserted into a conserved hydrophobic
326 pocket, and localizes to an α-helix at the XPB contact site with the p44 N-terminal
327 extension (Figure 3 – figure supplement 2I). This mutation is likely to impair the
328 stability and folding of the XPB NTD. Unlike T119P, this mutation leads to
329 impaired DNA opening in NER assays, reduced interaction with p52, reduced
330 ATPase activity (Coin et al., 2007), and strong impairment in DNA damage repair
331 (Riou et al., 1999), suggesting a severe effect on the structure of the XPB NTD.
332
333 Natural and synthetic mutations in the *Drosophila melanogaster* homolog of p52
334 that lead to disease-like phenotypes in flies and have similar defects when

335 introduced into human cells (Fregoso et al., 2007) map directly to the p52-XPB
336 interface, explaining their detrimental phenotypes (Figure 3C, Figure 3 – figure
337 supplement 2A).
338
339 Our structure assigns XPB residues 165-300 to a DRD-like domain that connects
340 the NTD to the RecA-like domain (Figure 3A, Figure 3 – figure supplement 1A),
341 the deletion of which is lethal in yeast (Warfield et al., 2016). The DRD is a DNA-
342 binding domain found in DNA repair enzymes and chromatin remodelers (Mason
343 et al., 2014; Obmolova et al., 2000) and has been implicated in DNA damage
344 recognition in archaeal XPB (Fan et al., 2006; Rouillon & White, 2010). Our 3.7 Å-
345 resolution map of TFIIH reveals that in eukaryotic XPB, one β-strand of the DRD
346 of archaeal XPB is replaced by an insertion of approximately 70 residues that
347 exhibits relatively low sequence conservation (Figure 3E, Figure 3 – figure
348 supplement 1B) and shifts the domain boundaries of the human XPB DRD-like
349 domain with respect to previous sequence alignments (Fan et al., 2006;
350 Oksenych et al., 2009). The part of this insertion resolved in our map consists of
351 a negatively charged linker and an α-helical element that contacts XPD directly
352 (Figure 3E, F). The surface on XPD involved in this interaction has been
353 implicated in the initial step of DNA substrate binding by XPD (Constantinescu-
354 Aruxandei et al., 2016; Kuper et al., 2012). Density features and secondary
355 structure prediction indicate the presence of several aromatic side chains of XPB
356 near the interface (Figure 3E), where they might form contacts resembling those
357 of nucleoside bases of XPD-bound DNA substrates (Figure 3F). Thus, XPB may
358 modulate substrate binding by XPD, further reinforcing the idea that XPD activity
359 is regulated by several other components of TFIIH.

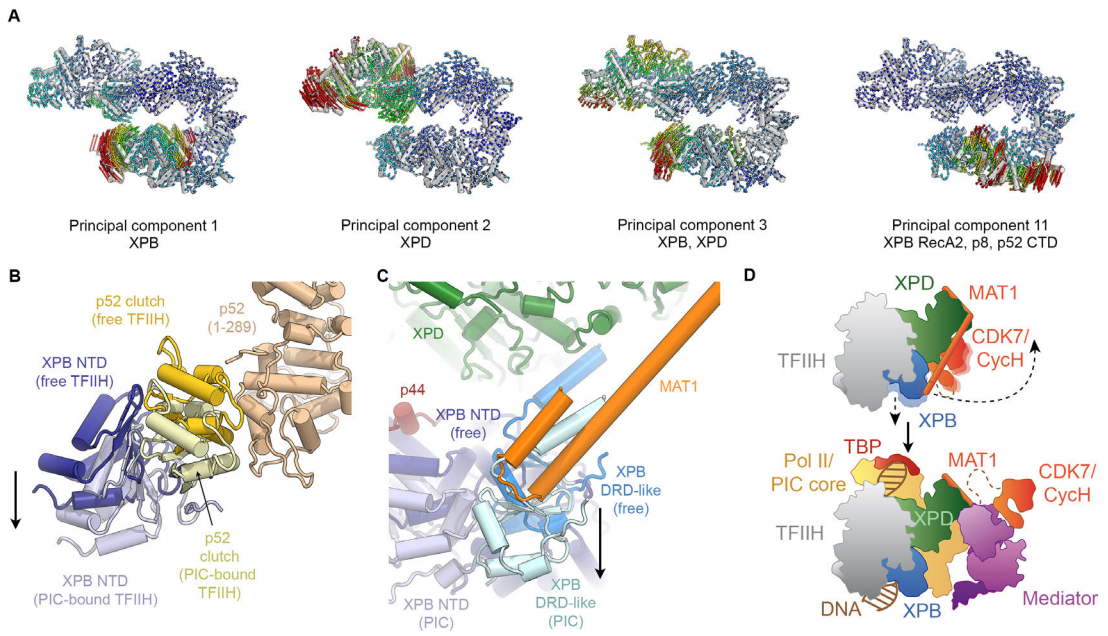

Figure 4. Conformational dynamics of TFIIH. (**A**) Results of multibody analysis. Several major modes of motion involve the enzymatic subunits of the TFIIH core complex or their domains. (**B**) Motion of the p52 clutch domain (closed conformation gold, open conformation light yellow) and associated XPB NTD (closed conformation blue, open conformation light blue) relative to the remainder of p52 (brown), based on comparison of free and PIC-bound TFIIH structures. (**C**) XPB motions from the closed conformation (free TFIIH; darker blue hues) and the open conformation (TFIIH-PIC; lighter hues). The MAT1-XPB contact dissociates during this rearrangement. (**D**) Schematic model for the conformational transitions in MAT1 and repositioning of the CAK kinase module during Pol II-PIC entry of TFIIH.

Figure supplement 1. Analysis of the conformational variance of TFIIH.

Figure supplement 2. Conformational dynamics of TFIIH and comparison with the PIC-bound TFIIH.

Conformational dynamics of the TFIIH core complex

In order to investigate the dynamics of TFIIH, we analyzed the conformational landscape of the particles in our cryo-EM dataset (Figure 4A, Figure 4 – figure supplement 1) (Nakane et al., 2018). This analysis revealed the relative motions

382 of the two ATPases and their domains (Figure 4A). The major mode of motion,
383 which involves the breaking of the interaction between XPB and XPD, resembles
384 the conformational transition of TFIIH when it enters the Pol II-PIC and binds to
385 DNA (Greber et al., 2017; He et al., 2016; Schilbach et al., 2017) (Figure 4 – figure
386 supplement 2A-C). Analysis of our TFIIH structure and comparison with that of
387 the complex within the Pol II-PIC maps (He et al., 2016; Schilbach et al., 2017)
388 allowed us to identify a specific rearrangement at the interface between the
389 clutch and adjacent winged helix domain in p52 (Figure 4B) as the basis of this
390 conformational change. A structural unit composed of XPB, p8 and the clutch
391 domain of p52 undergoes a downward motion upon DNA-binding within the Pol
392 II-PIC (Figure 4B, Figure 4 – figure supplement 2B, C). This conformational
393 change in TFIIH upon PIC entry also appears to break the interaction between
394 MAT1 and the XPB DRD-like domain (Figure 4C), which in turn might serve to
395 enable positioning of the CDK7-cyclin H dimer within the CAK subcomplex at the
396 appropriate location for Pol II-CTD phosphorylation in the mediator-bound Pol
397 II-PIC (Figure 4D) (Schilbach et al., 2017). Our structural comparison also reveals
398 that a TFIIE-XPB interaction that has been implicated in XPB regulation
399 (Schilbach et al., 2017) may depend on the existence of the open conformation of
400 TFIIH, as there would be steric hindrance in a complex involving the closed
401 conformation of TFIIH (Figure 4 – figure supplement 2D-F).
402
403 **Structure of XPD**
404
405 The structure of XPD shows the conserved domain arrangement of two RecA-like
406 domains (RecA1 and RecA2), with the FeS and ARCH domain insertions in RecA1
407 (Constantinescu-Aruxandei et al., 2016; Fan et al., 2008; Kuper et al., 2012). The
408 quality of the map allowed us to interpret the density for the N- and C-termini of
409 XPD, which closely approach each other near the nucleotide-binding site within
410 RecA1 (Figure 5A). The N-terminus of XPD forms a short two-stranded β-sheet
411 near the nucleotide-binding site in XPD RecA1 (which is empty in our structure)
412 and may contribute to the stabilization of the bound nucleotide via the aromatic
413 side chains of Y14 and Y18, the latter being affected by the Y18H mutation in an
414 XP/TTD patient (Kralund et al., 2013) (Figure 5 – figure supplement 1A-C). The

415 XPD C-terminal segment runs along the side of XPD RecA2 and interacts with the
416 linker between RecA1 and RecA2 (Figure 5 – figure supplement 1D). The C-
417 terminal segment includes the site of the K751Q polymorphism (Figure 5 – figure
418 supplement 1D), and deletion of this terminal segment causes XP in human
419 patients (Cleaver et al., 1999).
420

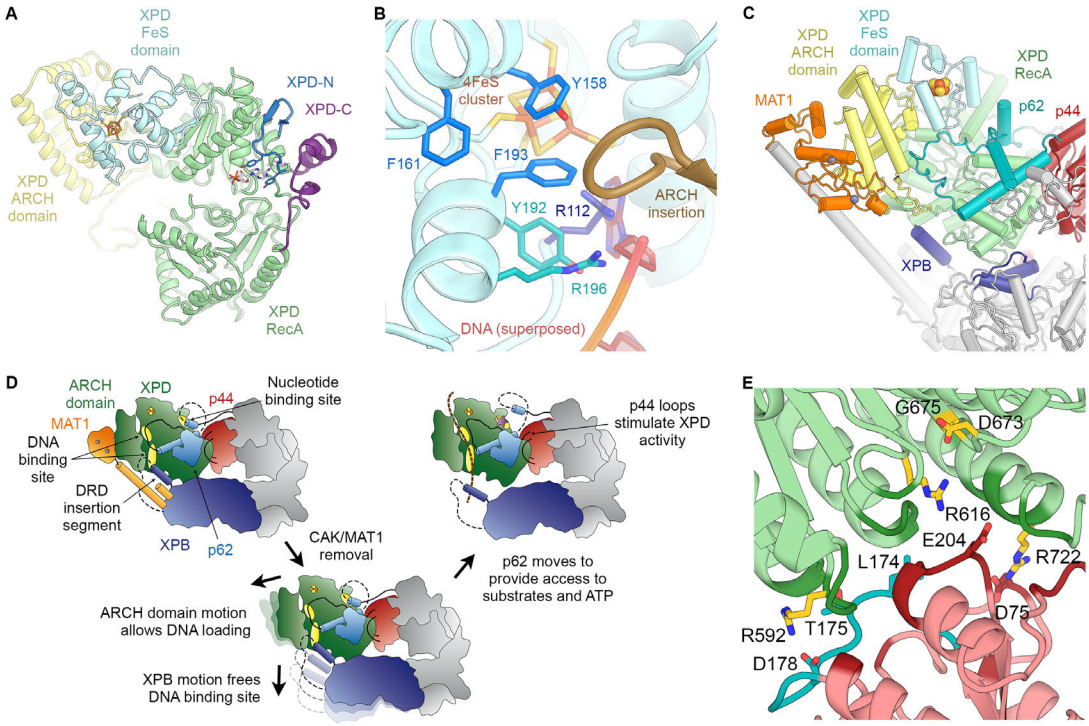

421

422 **Figure 5. Structure and regulation of XPD.** (**A**) Structure of XPD colored by
423 domain. N- and C-terminal segments (blue and purple, respectively) of XPD are
424 indicated. An ADP molecule (superposed from (Nguyen et al., 2013)) denotes the
425 nucleotide-binding pocket in XPD RecA1, which is empty in our structure. (**B**)
426 Structure of the FeS domain. Residues critical for XPD enzymatic activity (blue)
427 and damage verification (teal) are indicated. The R112H mutation causes TTD in
428 human patients. ARCH domain insertion brown. DNA superposed from (Büttner
429 et al., 2007). (**C**) Interaction network of XPD with surrounding TFIIH subunits
430 (interacting regions colored, remainder grey). (**D**) Cartoon model for repression
431 and de-repression of XPD by MAT1, XPB, and p62. (**E**) XPD-p44 interacting
432 regions (defined as residues within < 4 Å of the neighboring protein) are colored
433 in dark green (XPD) and dark red (p44). Residues discussed in the text are
434 shown as sticks; those with mutation data (natural variants or experimental

435 constructs) are colored yellow on XPD, teal on p44. The remainder of the β4-α5
436 loop harboring the synthetic p44 mutations is colored teal as well.
437
438 **Figure supplement 1.** Structure of XPD.
439 **Figure supplement 2.** XPD-p44 interaction.
440
441 Before XPD-bound DNA reaches the helicase motifs in the RecA like domains, it
442 passes through a pore-like structure next to the 4FeS cluster at the interface
443 between the FeS and ARCH domains (Figure 5 – figure supplement 1E, F) (Cheng
444 & Wigley, 2018; Constantinescu-Aruxandei et al., 2016; Kuper et al., 2012; Liu et
445 al., 2008; Wolski et al., 2008). This region was poorly defined in previous TFIIH
446 reconstructions, but our cryo-EM map now shows side-chain densities for the
447 aromatic residues Y158, F161, and F193, which are critical for the DNA-binding,
448 ATPase, and helicase activities of XPD (Kuper et al., 2014), as well as for residues
449 Y192 and R196, which form part of a DNA lesion recognition pocket (Mathieu et
450 al., 2013) (Figure 5B). This functionally important region is only partially
451 conserved in archaeal XPD homologs (Figure 5 – figure supplement 1G-I) (Fan et
452 al., 2008; Kuper et al., 2012; Wolski et al., 2008). A eukaryotic-specific loop
453 insertion in the XPD ARCH domain (Greber et al., 2017; Schilbach et al., 2017)
454 closely approaches this binding pocket (Figure 5B) and may serve to regulate the
455 binding of DNA in the lesion recognition pocket such as to prevent untimely
456 access of substrates to the XPD pore.
457
458 **Interactions and regulation of XPD**
459
460 Our structure of TFIIH shows that XPD forms architectural and regulatory
461 interactions with four other TFIIH subunits: XPB, p62, p44, and MAT1, which
462 together form a cradle-like structure around XPD (Figure 5C). We described
463 above two interactions that could potentially regulate XPD activity: the newly
464 defined interaction of an insertion element in the XPB DRD with a DNA-binding
465 site in XPD (Figure 3E, F); and XPD-p62 interactions involving the XPD
466 nucleotide binding pocked and DNA binding cavity (Figure 2, Figure 2 – figure
467 supplement 1D-F) that implicate p62, as well as XPB, in XPD regulation.

468 Additionally, it is known that the helicase activity of XPD is inhibited by the CAK
469 subcomplex (Araújo et al., 2000; Sandrock & Egly, 2001). The contacts we see
470 between MAT1 and XPD localize to the ARCH domain of XPD and the N-terminal
471 RING domain and helical bundle of MAT1 (residues 1-210) (Figure 5C), in
472 agreement with previous structural (Greber et al., 2017; Schilbach et al., 2017)
473 and biochemical analysis (Abdulrahman et al., 2013; Luo et al., 2015; Warfield et
474 al., 2016). The interaction between the XPD ARCH domain and the MAT1 helical
475 bundle is characterized by charge complementarity (Figure 5 – figure
476 supplement 1J-M). This interface is highly dynamic, enabling the release of MAT1
477 and the entire CAK subcomplex from TFIIH during NER, as well as its subsequent
478 re-association to regenerate a transcription-competent TFIIH (Coin et al., 2008).
479
480 Insertion of substrate DNA into the pore between the XPD ARCH and FeS
481 domains requires the flexibility of the XPD ARCH domain (Constantinescu-
482 Aruxandei et al., 2016), and large domain motions have been observed in the
483 structure of the DNA-bound homologous helicase DinG upon nucleotide binding
484 (Cheng & Wigley, 2018). This suggests a role for the mobility of the ARCH
485 domain in both DNA loading and DNA translocation by the XPD helicase. Our
486 structure suggests that binding of the MAT1 helical bundle and RING domain to
487 the ARCH domain may prevent such motion and therefore the subsequent
488 substrate loading and XPD helicase activity (Figure 5D), in agreement with
489 biochemical data that show XPD inhibition upon MAT1 binding (Sandrock &
490 Egly, 2001), as well as reduced single-stranded DNA affinity of TFIIH in the
491 presence of the CAK (Li et al., 2015). Conversely, release of MAT1 from XPD
492 might allow the ARCH domain to move more freely, thereby de-repressing XPD.
493 Furthermore, displacement of the MAT1 α-helix that connects XPD to XPB may
494 allow XPB to move away from XPD, thereby unmasking the substrate-binding
495 site on XPD RecA2 that is otherwise occluded by the DRD insertion element
496 (Figure 5D). This latter conformational change would be similar, overall, to that
497 seen for TFIIH upon incorporation into the Pol II-PIC, where XPD and XPB move
498 apart and density for the MAT1 helix is missing (Figure 4C) (He et al., 2016;
499 Schilbach et al., 2017). We propose that the combined unmasking of the XPD
500 substrate binding site and the enhanced flexibility of the XPD ARCH domain may

501 both contribute to de-repression of the XPD helicase upon release of MAT1. This
502 mechanism of XPD inhibition by MAT1 does not exclude the possibility of
503 additional repression of NER activity by the CAK subcomplex through
504 phosphorylation of NER pathway components (Araújo et al., 2000).
505

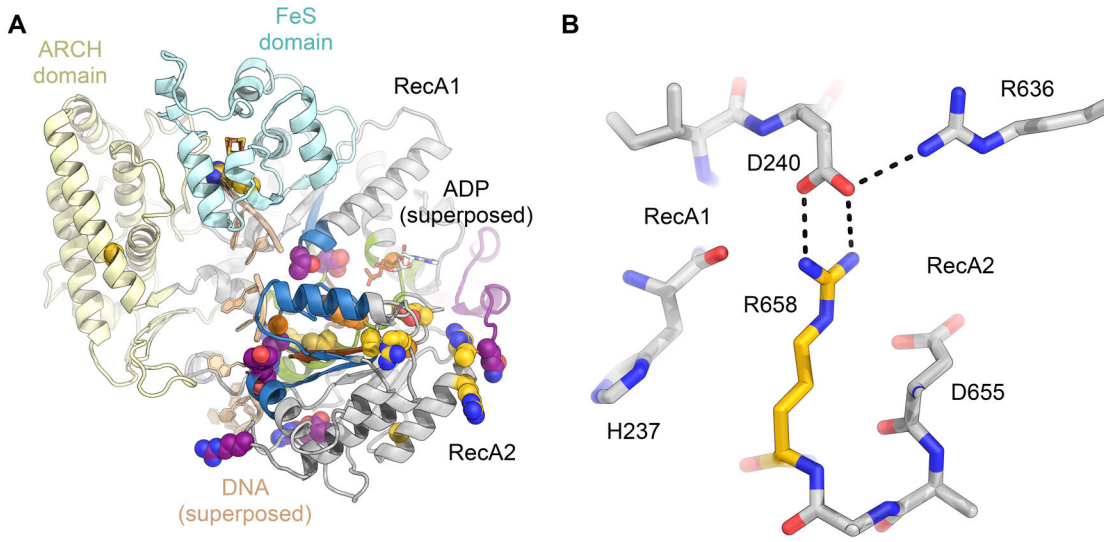

506
507 **Figure 6. Disease mutations in XPD.** (**A**) Residues affected by disease
508 mutations are shown as spheres (XP purple; TTD yellow; CS-XP orange).
509 Conserved helicase elements for DNA binding are shown in blue, for nucleotide
510 binding and hydrolysis in green, and for coupling of nucleotide hydrolysis and
511 DNA translocation in brown. DNA superposed from (Büttner et al., 2007). (**B**)
512 Salt bridge between R658 (RecA2) and D240 (RecA1) visualized in our structure
513 that is affected by the temperature sensitive TTD mutation R658C (Vermeulen et
514 al., 2001).
515
516 **Figure supplement 1.** Mapping of XPD disease mutations on the TFIIH
517 structure.
518
519 Our structure also resolves in detail the XPD-p44 interaction, a known regulatory
520 interface (Dubaele et al., 2003; Kim et al., 2015; Kuper et al., 2014) affected by
521 numerous disease mutations (Cleaver et al., 1999; Greber et al., 2017; Kuper et
522 al., 2014) (Figure 5E). The relatively small interaction surface between p44 and
523 XPD, of just 1010 Å^2 (Figure 5 – figure supplement 2A), contrasts with the much
524 larger buried surface of 3370 Å^2 between XPD and p62, or 1570 Å^2 for the p52-

525 XPB interaction. This smaller interaction surface may result in higher sensitivity
526 to mutations that localize at the XPD-p44 interface. Our structure, thus,
527 rationalizes the deleterious effect of a number of natural and synthetic mutations
528 in this interface (Supplementary Note 1, Figure 5 – figure supplement 2B-E),
529 including mutations L174W and T175R in the β4-α5 loop of p44 (Figure 5E)
530 (Kim et al., 2015; Seroz et al., 2000), which may lead to steric clashes in the
531 densely packed interface (Figure 5 – figure supplement 2B), and the XPD R722W
532 mutation (Kuper et al., 2014), which disrupts the salt bridge with D75 in p44 and
533 may additionally cause steric clashes with neighboring p44 residues due to the
534 bulky tryptophan side chain (Figure 5 – figure supplement 2C). Our structure
535 also shows that, in contrast to a previously proposed model (Luo et al., 2015),
536 the XPD R616P, D673G, and G675R disease mutations act either via disruption of
537 the XPD structure or the XPD-p44 interface, but not via disruption of the
538 interaction with p62 (see Supplementary Note 1, Figure 5 – figure supplement
539 2D). Notably, the p44-dependet stimulation of XPD activity does not depend on
540 the presence of p62 (Dubaele et al., 2003; Kim et al., 2015; Kuper et al., 2014).
541 We were also able to map a number of disease mutations onto our XPD structure
542 (Figure 6A) and analyze in detail the interactions involving the affected residues
543 (example shown in Figure 6B). Our analysis confirms that XP mutations mostly
544 localize near the helicase substrate-binding or active sites, while TTD mutations
545 predominantly localize to the periphery of XPD (Figure 6, Figure 6 – figure
546 supplement 1) (Fan et al., 2008; Liu et al., 2008), where they disrupt TFIIH
547 assembly and cause the transcription defects that are a hallmark of this disease
548 (Dubaele et al., 2003) (Supplementary Note 2).
549
550 **DISCUSSION**
551
552 Our study reveals the complete structure of the TFIIH core complex and provides
553 mechanistic insights into the regulation of its two component helicases.
554 Specifically, it shows XPD wrapped by numerous interactions with XPB, p62, p44,
555 and MAT1 (Figure 5C, D), indicating how its activity can be tightly controlled and
556 de-repressed only when its enzymatic function is needed. XPD activity is not
557 needed and most likely inhibited during transcription initiation, but it may also

558 be tightly controlled during NER, when repair bubble opening and lesion
559 verification need to be coordinated with the recruitment and activation of the
560 damage recognition and processing machinery (Figure 7 and Discussion). While
561 the regulation of XPD by MAT1 and p44 has been studied in some detail, and the
562 domain motions in TFIIH suggest a straightforward mechanism for liberating the
563 substrate-binding site on XPD RecA2, less was known about the interplay
564 between XPD and p62. Our structure now shows how p62 is able to impede both
565 substrate and nucleotide binding in XPD RecA1, and hints at dynamic structural
566 changes of p62 during de-repression and enzymatic activity of XPD, possibly
567 regulated by other components of the transcription or NER pathways.
568

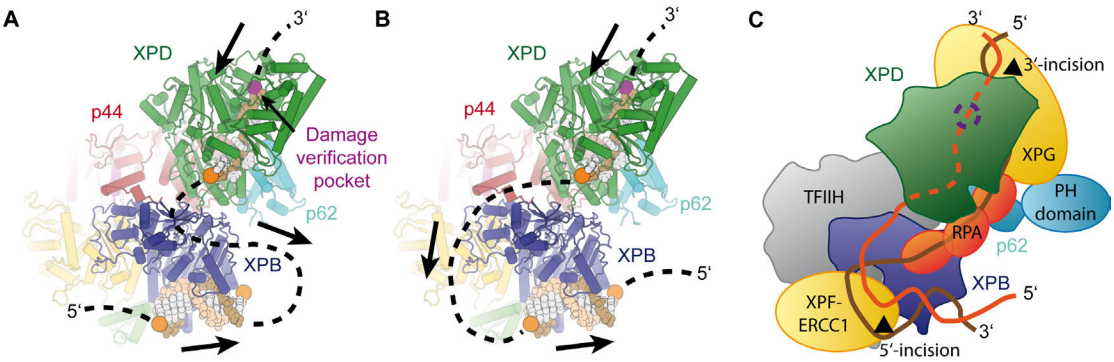

569
570 **Figure 7. Implications for assembly of the repair bubble during NER.** (**A**)
571 Schematic of DNA-bound TFIIH (DNA damage verification pocket in XPD and
572 DNA 5'-phosphates indicated by purple and orange spheres, respectively)
573 Binding of both XPB and XPD to the damaged strand would lead to extrusion of a
574 bubble when XPD scans in the 5'-3' direction, while XPB may be stationary or
575 contribute to bubble extrusion if translocating in the 3'-5' direction (DNA
576 superposed from PDB IDs 5H8W, 2P6R, 5OQJ (Büttner et al., 2007;
577 Constantinescu-Aruxandei et al., 2016; Schilbach et al., 2017)). (**B**) Binding of
578 XPB to the undamaged strand would enable the entire complex to scan in 5'-3'
579 direction, given the opposing polarities of the two ATPases/helicases involved.
580 (**C**) Model for the assembled repair bubble. Positions of NER factors are
581 approximate. See Discussion for details.
582
583

584 Our results allow us to put extensive biochemical data on the NER pathway into a
585 structural context (Figure 7). Depending on whether XPB binds to the damaged
586 (Figure 7A) or undamaged (Figure 7B) strand, the combined action of XPD and
587 XPB could lead to the extrusion of a DNA bubble (Figure 7A) or to the tracking of
588 the entire complex towards the lesion (Figure 7B), which is initially located 3' of
589 the TFIIH binding site (Sugasawa et al., 2009). The latter hypothesis is attractive
590 in the context of biochemical data that show that XPD tracks along the damaged
591 strand in the 5' to 3' direction until it encounters the DNA lesion in order to
592 verify the presence of a bona fide NER substrate (Buechner et al., 2014; Li et al.,
593 2015; Mathieu et al., 2013; Naegeli et al., 1993; Sugasawa et al., 2009; Wirth et
594 al., 2016). It is worth noting that the length of DNA fragments excised during
595 NER is approx. 29 nt, with 22 nt located 5' and 5 nt located 3' of a thymine dimer
596 lesion (Huang et al., 1992). According to our structure, the 22 nt 5'-fragment
597 corresponds well to the estimated 20 nt of DNA that are required to span the
598 distance from the DNA damage verification pocket in XPD (Mathieu et al., 2013)
599 to the helicase elements of XPB. This proposal is compatible with a model in
600 which TFIIH sitting on the open repair bubble might track towards the lesion,
601 where it would stop due to inhibition of XPD (Li et al., 2015; Mathieu et al., 2013;
602 Naegeli et al., 1993), at which point double incision could be initiated. However,
603 this model (Figure 7B) would require strong DNA bending before both XPB and
604 XPD could be loaded. Additionally, it has not been fully resolved whether XPB
605 participates in DNA translocation or unwinding during TFIIH activity in NER (Li
606 et al., 2015), which would be required in the tracking model (Li et al., 2015), or
607 whether it exclusively acts to anchor the complex in the vicinity of the DNA
608 lesion (Coin et al., 2007; Oksenych et al., 2009). Independently of the orientation
609 of the repair bubble, our structural data are compatible with literature data
610 introduced above and a model that localizes XPG near XPD and p62 (site of 3'-
611 incision), XPF-ERCC1 near XPB (site of 5'-incision), and with RPA binding the
612 non-damaged strand (Figure 7C). We have currently not included XPA in this
613 model because its interactions with distinct partners or participation in various
614 processes, such as involvement in CAK release (Coin et al., 2008), binding to p8
615 (Ziani et al., 2014), and participation in helicase stalling after lesion recognition

616 (Li et al., 2015), suggest its localization to various, often distant sites on TFIIH, or
617 the repair bubble in general (Sugitani et al., 2016).
618
619 In summary, our structure of the human TFIIH core complex reveals the
620 interactions that govern the architecture and function of this molecular machine,
621 provides new insights into the regulation of its enzymatic subunits, and thus
622 constitutes an excellent framework for further mechanistic studies of TFIIH in
623 the context of larger DNA repair and transcription assemblies.
624
625 **METHODS**
626
627 **TFIIH purification, cryo-EM specimen preparation, and data collection**
628
629 TFIIH was purified and cryo-EM grids were prepared on carbon-coated C-flat CF
630 4/2 holey carbon grids (Protochips) using a Thermo Fisher Scientific Vitrobot
631 Mk. IV, as previously described (Greber et al., 2017). To improve on our previous
632 4.4 Å cryo-EM map of human TFIIH (Greber et al., 2017), which was based on 4
633 cryo-EM datasets (3 of which were retained in the 4.4 Å reconstruction, datasets
634 8-10 in Supplementary Table 1) from a Titan microscope (Thermo Fisher
635 Scientific) equipped with a side-entry holder (Gatan) and a K2 Summit direct
636 electron detector (Gatan), we collected new data (dataset 7 in Supplementary
637 Table 1) on a Titan KRIOS microscope (Thermo Fisher Scientific) operated at 300
638 kV extraction voltage and equipped with a C_S-corrector, a K2 Summit direct
639 electron detector (Gatan) operated in super-resolution counting mode, and a
640 Quantum energy filter (Gatan). This dataset was collected under the same
641 imaging conditions as our previous data (i.e. 37,879 x magnification resulting in
642 1.32 Å pixel size, and at a total exposure of 40 e^- $Å^{-2}$), except for the change of
643 microscope. Datasets 7-10 could be combined to yield a cryo-EM map at 4.3 Å
644 resolution (not shown), however, this did not lead to a substantial improvement
645 in map quality, suggesting that particle alignment quality was limiting. We
646 therefore opted to collect further data on a Titan KRIOS electron microscope
647 (Thermo Fisher Scientific) operated at 300 kV acceleration voltage and equipped
648 with a Volta Phase Plate (VPP), a Gatan Quantum energy filter (operated at 20 eV

649 slit width), and a Gatan K2 Summit direct electron detector (operated in super-
650 resolution counting mode). VPP data (datasets 1-6 in Supplementary Table 1)
651 were collected according to the defocus acquisition technique (Danev &
652 Baumeister, 2017; Khoshouei et al., 2017) at 43,478 x magnification, resulting in
653 a physical pixel size of 1.15 Å on the object scale, with a total electron exposure
654 of 50 e^{-} $Å^{-2}$ at an exposure rate of 6.1 e^{-} $Å^{-2}$ s^{-1} during an exposure time of 8.25 s,
655 dose fractionated into 33 movie frames (50 frames for dataset 6). Data collection
656 was monitored on-the-fly using FOCUS (Biyani et al., 2017) to ensure proper
657 evolution of the VPP-induced phase shift.
658
659 **Cryo-EM data processing**
660
661 Initially, we used data collected in 10 microscopy sessions, 6 sessions using the
662 VPP and 4 sessions without the VPP, resulting in > 30'000 total micrographs, of
663 which approx. 15,000 were retained after inspection of the quality of Thon rings
664 and CTF fitting (for details, see Supplementary Table 1). Movie stacks were
665 aligned and dose weighed using MOTIONCOR2 (Zheng et al., 2017). The aligned,
666 dose weighed sums from the datasets collected at 1.32 Å pixel size (datasets 7-
667 10) were up-sampled to 1.15 Å per pixel to match the scale of the micrographs
668 collected using the VPP (datasets 1-6) after calibrating the two magnifications to
669 each other based on 3D reconstructions computed from the two types of data.
670 CTF parameters were estimated using GCTF (Zhang, 2016) and particles were
671 picked using GAUTOMATCH (Kai Zhang, MRC Laboratory of Molecular Biology,
672 Cambridge UK) or RELION (Scheres, 2015) using templates generated from a
673 preliminary run without reference templates. All subsequent data processing
674 was performed in RELION 2 (Kimanius et al., 2016; Scheres, 2012) or RELION 3
675 (Nakane et al., 2018).
676
677 To remove false positive particle picks and broken particles, initial 3D
678 classification was performed on each dataset individually (datasets 3, 4, 5), or on
679 a few pooled datasets if appropriate (datasets 1 and 2 were pooled as they used
680 the same batch of specimen; the non-VPP datasets 7-10 were joined because only
681 few micrographs were retained due to more stringent quality criteria compared

682 to our previous study; and dataset 6 was initially classified together with
683 particles from dataset 4 to compensate for particle orientation bias, see Figure 1
684 – figure supplement 1). In summary, a total of > 2,000,000 initial particle picks
685 were subjected to this initial 3D classification, identifying approx. 820,000 intact
686 particles that were subjected to further processing. After 3D auto-refinement and
687 another round of 3D classification, performed separately for the VPP and non-
688 VPP data because the two data types were spuriously separated into distinct
689 classes in combined RELION 3D classification runs, the best classes (one from
690 VPP and non-VPP data each) resulting from the high-resolution 3D classifications
691 were refined according to the gold-standard refinement procedure (fully
692 independent half-sets), resulting in a 3.9 Å-resolution reconstruction according
693 to the FSC = 0.143 criterion (Rosenthal & Henderson, 2003; Scheres & Chen,
694 2012). Beam tilt refinement in RELION 3 improved the map computed from the
695 VPP data to 3.7 Å resolution. The non-VPP data no longer improved the
696 reconstruction after beam tilt correction and was therefore discarded at this
697 point. The final map was post-processed by application of b-factor of -175 A^2 and
698 low-pass filtration to the nominal 3.7 Å resolution for visualization and later
699 coordinate refinement.
700
701 To facilitate the interpretation of less ordered or only partially occupied parts of
702 the structure, including the p62 BSD2 domain, the MAT1 RING domain, the MAT1
703 three-helix bundle at the XPD arch domain, and the N-terminus of XPD, we used
704 signal subtracted classification (Bai et al., 2015; Nguyen et al., 2015) (p62 BSD2
705 domain, Figure 1 – figure supplement 3), focused classification (MAT1 RING
706 domain, Figure 1 – figure supplement 4), and multibody refinement (Nakane et
707 al., 2018) (MAT1 three-helix bundle and XPD N-terminus, Figure 1 – figure
708 supplement 5). For these classification procedures, we used only the VPP data
709 because 3D classification separated VPP and conventional cryo-EM data into
710 distinct classes, rendering combined classification ineffective. Multibody
711 refinement led to only a slight improvement in resolution (to 3.6 Å) relative to
712 the overall refined best map, and only during the first two iterations, likely due
713 to the relatively small size of the individual bodies and the resulting limited
714 signal for alignment. However, the above-mentioned structural elements showed

715 improved density features (Figure 1 – figure supplement 1B) and could be more
716 reliably interpreted in the multibody-refined XPD-MAT1 map (green in Figure 1
717 – figure supplement 5; also used in Figure 1 – figure supplement 2E, F). Overall,
718 the use of VPP data in this work resulted in substantial improvements both in
719 nominal resolution (Figure 1 – figure supplement 2D) and map quality (Figure 1
720 – figure supplement 2E-G) compared to our previous 4.4 Å-resolution structure.
721
722 **Model building and refinement**
723
724 The previous structure of the human TFIIH core complex (Greber et al., 2017)
725 and of yeast TFIIH in the Pol II-PIC (Schilbach et al., 2017) were docked into the
726 cryo-EM map and used as the basis for atomic modeling in O (Jones et al., 1991)
727 and COOT (Emsley et al., 2010). In addition to these models, the structure of the
728 human p34 VWFA-p44 RING domain complex (Radu et al., 2017), the N-terminal
729 RING domain of MAT1 (Gervais et al., 2001), the C-terminal RecA-like domain of
730 human XPB (Hilario et al., 2013) and several homology models for the p52
731 winged-helix domains generated using the PHYRE2 web server (Kelley et al.,
732 2015) based on templates PDB IDs 3F6O and 1STZ (Liu et al., 2005) were used
733 for model building.
734
735 *Building of 52:* The structure of p52 was traced and built completely *de novo*,
736 with the exception of the winged-helix domains and the very C-terminal domain,
737 where a homology model was placed into the cryo-EM map together with the p8
738 structure (Kainov et al., 2008; Vitorino et al., 2007) and adjusted to the density.
739
740 *XPB:* The structure of the XPB NTD was also built *de novo*, the structure of the
741 DRD was extensively re-built, and the RecA-like domains were rebuilt to improve
742 the fit to the density.
743
744 *XPD:* The improved cryo-EM map enabled detailed re-building of XPD, including
745 correction of register shifts in the more poorly ordered regions of the protein
746 and extension of the termini.
747

748 *MAT1:* The N-terminal MAT1 RING domain (Gervais et al., 2001) was first docked
749 into the focused classified density and combined with the rest of the TFIIH
750 model, were it helped guide the assignment of the sequence register to the MAT1
751 model, in combination with density features of large side chains in the helical
752 regions.
753
754 *Building of p34:* The human p34 structure (Radu et al., 2017) was docked into the
755 map as is, extended near the interaction site with p52, and combined with a
756 completely re-built model of the C-terminal eZnF domain (Schilbach et al., 2017).
757
758 *Building of p44:* The p44 VWFA fold needed only minor rebuilding and was
759 combined with the eZnF domain and the C-terminal human RING domain model
760 (Radu et al., 2017; Schilbach et al., 2017). The p44 NTE was built according to the
761 density at the contact site with XPB and guided by CX-MS data (Luo et al., 2015).
762 Both the features of the cryo-EM map and crosslinks of the p44 NTE to p34, p52,
763 and XPB (Figure 1 – figure supplement 6E) unambiguously confirm the tracing of
764 this segment towards the XPB NTD, rather than alternative tracing towards XPD
765 (this density is now assigned to p62, in agreement with p62-XPD crosslinks; see
766 below and Figure 1 – figure supplement 6G).
767
768 *Building of p62:* The p62 protein was modeled based on the placement of the BSD
769 domains (PDB ID 2DII), secondary structure prediction, extension of docked
770 coordinates (Greber et al., 2017; Schilbach et al., 2017), and new tracing of the
771 protein chain. Placement of the regions near XPD, where density is weak overall,
772 was guided by matching the succession of secondary structure elements along
773 the p62 sequence with helical densities in the cryo-EM map (Figure 2 – figure
774 supplement 1A), and corroborated by CX-MS data (Luo et al., 2015), which
775 showed excellent agreement of p62-XPD crosslinking data with the structure
776 (Figure 1 – figure supplement 6G). Crosslinks between p62 and p44 showed a
777 relatively large proportion of outliers (Supplementary Data Table 1), which may
778 be due to the fact that the sequence register of the p62 segments to which these
779 crosslinks map is not well constrained. These segments were modeled as poly-
780 alanines and deposited without sequence assignment (UNK; Supplementary

781 Table 2). Maps low-pass filtered to 6 Å and sharpened by a b-factor of only -100
782 $Å^2$ were used to guide docking of domains and assess the continuity of the
783 density in poorly ordered regions of the protein (Figure 2 – figure supplement
784 1B, C).
785
786 The resulting coordinate model (Supplementary Table 2) was refined using the
787 real space refinement program in PHENIX (Adams et al., 2010; Afonine et al.,
788 2018) and validated using the MTRIAGE program in PHENIX and the
789 MOLPROBITY web server (Chen et al., 2010). Ramachandran, C_β, rotamer, and
790 secondary structure restraints were used throughout the refinement to ensure
791 good model geometry at the given resolution. Data used in the refinement
792 excluded spatial frequencies beyond the nominal 3.7 Å resolution of the cryo-EM
793 map to prevent over-fitting. The N-terminal RING domain of MAT1 and the BSD1
794 domain of p62, for which only poorly resolved density is present in the final
795 cryo-EM map, were additionally restrained by reference restraints (Headd et al.,
796 2012) using the NMR structures of the corresponding domains (PDB ID 1G25
797 and 2DII, respectively) (Gervais et al., 2001). The side chains of these two
798 domains (with the exception of residues involved in zinc finger formation and of
799 prolines) were truncated at the Cβ position to reflect the lower resolution of the
800 corresponding densities. The FSC curve between the refined coordinate model
801 and the cryo-EM map extends to 3.9 Å and the distribution of b-factors in the
802 refined coordinate model (Figure 1 – figure supplement 2C) mirror the local
803 resolution of the cryo-EM map (Figure 1 – figure supplement 2D), as expected.
804 Refinement statistics are given in Supplementary Table 3 and are typical for
805 structures in this resolution range (97th and 99th percentiles for MOLPROBITY
806 clash score and overall score (Chen et al., 2010)).
807
808 **Flexibility analysis**
809
810 For the analysis of conformational dynamics of TFIIH, VPP datasets 1 and 2 were
811 subjected to multibody refinement in RELION 3 (Nakane et al., 2018) using 6
812 masks (Figure 4 – figure supplement 1). The volume series for the first 16
813 principal components were reconstructed and difference densities (green and

purple in Figure 4 – figure supplement 1) were computed between the most extreme states in each series (blue and yellow in Figure 4 – figure supplement 1). Subsequently, roughly 20,000 particles corresponding to both ends of the distribution were used for selected principal components and subjected to 3D refinement, resulting in maps of approx. 10 Å resolution. The refined atomic model of the TFIIH core complex, subdivided into suitable rigid bodies, was then rigid-body refined into these volumes using PHENIX real space refinement (Afonine et al., 2018) and coordinate displacement between the two resulting models for each principal component was plotted to obtain an initial assessment of the modes of motion present in the TFIIH dataset (Figure 4A). For actual structural interpretation (Figure 4B, C), the final cryo-EM maps of the TFIIH core complex (this work) and TFIIH in the context of the Pol II-PIC (Schilbach et al., 2017) were used.

Other

Figures were created using PyMol (The PyMOL Molecular Graphics System, Version 1.8 Schrödinger, LLC.) and the UCSF Chimera package from the Computer Graphics Laboratory, University of California, San Francisco (supported by NIH P41 RR-01081) (Pettersen et al., 2004). Protein-protein interface statistics were determined using PISA (Krissinel & Henrick, 2007).

ACKNOWLEDGMENTS

We thank D. Wigley for sharing of structural data, S. Scheres for sharing computer code before publication, R. Tjian, S. Zheng, and D. King for supplying XPB mAB and peptides for TFIIH purification, P. Grob and A. Chintangal for support with microscopy and computing, respectively, and Z. Yu and C. Hong for data collection at the Janelia farm cryo-EM facility. We acknowledge the use of the resources of the National Energy Research Scientific Computing Center (NERSC), a DOE Office of Science user facility supported by the Office of Science of the U.S. Department of Energy under Contract No. DE-AC02-05CH11231.

847 **ADDITIONAL INFORMATION**

848

849 **Funding**

850

851 This work was funded through NIGMS grants R01-GM63072 and P01-GM063210
852 to E.N.. B.J.G. was supported by fellowships from the Swiss National Science
853 Foundation (projects P300PA_160983, P300PA_174355). E.N. is a Howard
854 Hughes medical investigator.

855

856 **Author contributions**

857

858 E.N. directed the study. J.F. performed HeLa cell culture and purified TFIIH. B.J.G.
859 performed cryo-EM specimen preparation, data processing, atomic model
860 building, and coordinate refinement. D.B.T and B.J.G collected the cryo-EM data.
861 B.J.G. wrote the initial draft of the manuscript and all authors contributed to the
862 final version.

863

864 **Supplementary Data Table 1 (separate file)**

865

866 Result summary of mapping of CX-MS data (Luo et al., 2015) onto the TFIIH
867 structure.

868

869 **REFERENCES**

870

871 Abdulrahman W., Iltis I., Radu L., Braun C., Maglott-Roth A., Giraudon C., Egly J.-
872 M., Poterszman A. (2013) ARCH domain of XPD, an anchoring platform for CAK
873 that conditions TFIIH DNA repair and transcription activities. *Proc Natl Acad Sci*
874 *USA* **110:** E633-642

875 Adams P. D., Afonine P. V., Bunkóczi G., Chen V. B., Davis I. W., Echols N., Headd J.
876 J., Hung L. W., Kapral G. J., Grosse-Kunstleve R. W. et al (2010) PHENIX: a
877 comprehensive Python-based system for macromolecular structure solution.
878 *Acta Crystallogr D Biol Crystallogr* **66:** 213-221

879 Afonine P. V., Poon B. K., Read R. J., Sobolev O. V., Terwilliger T. C., Urzhumtsev A.,
880 Adams P. D. (2018) Real-space refinement in PHENIX for cryo-EM and
881 crystallography. *Acta Crystallogr D Struct Biol* **74:** 531-544

882 Alekseev S., Nagy Z., Sandoz J., Weiss A., Egly J.-M., Le May N., Coin F. (2017)
883 Transcription without XPB Establishes a Unified Helicase-Independent
884 Mechanism of Promoter Opening in Eukaryotic Gene Expression. *Mol Cell* **65:**
885 504-513.e505

886 Araújo S. J., Tirode F., Coin F., Pospiech H., Syväoja J. E., Stucki M., Hübscher U.,
887 Egly J. M., Wood R. D. (2000) Nucleotide excision repair of DNA with
888 recombinant human proteins: definition of the minimal set of factors, active
889 forms of TFIIH, and modulation by CAK. *Genes & Dev* **14:** 349-359

890 Bai X.-C., Rajendra E., Yang G., Shi Y., Scheres S. H. (2015) Sampling the
891 conformational space of the catalytic subunit of human γ -secretase. *Elife* **4:**
892 e11182

893 Balasingham S. V., Zegeye E. D., Homberset H., Rossi M. L., Laerdahl J. K., Bohr V.
894 A., Tønjum T. (2012) Enzymatic activities and DNA substrate specificity of
895 Mycobacterium tuberculosis DNA helicase XPB. *PLoS ONE* **7:** e36960

896 Berico P., Coin F. (2017) Is TFIIH the new Achilles heel of cancer cells?
897 *Transcription* **9:** 47-51

898 Bienstock R. J., Skorvaga M., Mandavilli B. S., Van Houten B. (2003) Structural and
899 functional characterization of the human DNA repair helicase XPD by
900 comparative molecular modeling and site-directed mutagenesis of the bacterial
901 repair protein UvrB. *J Biol Chem* **278:** 5309-5316

902 Biyani N., Righetto R. D., McLeod R., Caujolle-Bert D., Castaño-Diez D., Goldie K.
903 N., Stahlberg H. (2017) Focus: The interface between data collection and data
904 processing in cryo-EM. *J Struct Biol* **198:** 124-133

905 Botta E., Nardo T., Lehmann A. R., Egly J.-M., Pedrini A. M., Stefanini M. (2002)
906 Reduced level of the repair/transcription factor TFIIH in trichothiodystrophy.
907 *Hum Mol Genet* **11:** 2919-2928

908 Buechner C. N., Heil K., Michels G., Carell T., Kisker C., Tessmer I. (2014) Strand-
909 specific recognition of DNA damages by XPD provides insights into nucleotide
910 excision repair substrate versatility. *J Biol Chem* **289:** 3613-3624

911 Busso D., Keriel A., Sandrock B., Poterszman A., Gileadi O., Egly J. M. (2000)
912 Distinct regions of MAT1 regulate cdk7 kinase and TFIIH transcription activities.
913 *J Biol Chem* **275:** 22815-22823

914 Büttner K., Nehring S., Hopfner K.-P. (2007) Structural basis for DNA duplex
915 separation by a superfamily-2 helicase. *Nat Struct Mol Biol* **14:** 647-652

916 Chen V. B., Arendall W. B., Headd J. J., Keedy D. A., Immormino R. M., Kapral G. J.,
917 Murray L. W., Richardson J. S., Richardson D. C. (2010) MolProbity: all-atom
918 structure validation for macromolecular crystallography. *Acta Crystallogr D Biol*
919 *Crystallogr* **66:** 12-21

920 Cheng K., Wigley D. B. (2018) DNA translocation mechanism of an XPD family
921 helicase. *Elife* **7**

922 Clarkson S. G., Wood R. D. (2005) Polymorphisms in the human XPD (ERCC2)
923 gene, DNA repair capacity and cancer susceptibility: an appraisal. *DNA Repair*
924 *(Amst)* **4:** 1068-1074

925 Cleaver J. E., Thompson L. H., Richardson A. S., States J. C. (1999) A summary of
926 mutations in the UV-sensitive disorders: xeroderma pigmentosum, Cockayne
927 syndrome, and trichothiodystrophy. *Hum Mutat* **14:** 9-22

928 Coin F., Marinoni J. C., Rodolfo C., Fribourg S., Pedrini A. M., Egly J. M. (1998)
929 Mutations in the XPD helicase gene result in XP and TTD phenotypes, preventing
930 interaction between XPD and the p44 subunit of TFIIH. *Nat Genet* **20:** 184-188

931 Coin F., Oksenych V., Egly J.-M. (2007) Distinct roles for the XPB/p52 and
932 XPD/p44 subcomplexes of TFIIH in damaged DNA opening during nucleotide
933 excision repair. *Mol Cell* **26:** 245-256

934 Coin F., Oksenych V., Mocquet V., Groh S., Blattner C., Egly J.-M. (2008) Nucleotide
935 excision repair driven by the dissociation of CAK from TFIIH. *Mol Cell* **31:** 9-20

936 Coin F., Proietti De Santis L., Nardo T., Zlobinskaya O., Stefanini M., Egly J.-M.
937 (2006) p8/TTD-A as a repair-specific TFIIH subunit. *Mol Cell* **21:** 215-226

938 Compe E., Egly J.-M. (2016) Nucleotide Excision Repair and Transcriptional
939 Regulation: TFIIH and Beyond. *Annu Rev Biochem* **85:** 265-290

940 Constantinescu-Aruxandei D., Petrovic-Stojanovska B., Penedo J. C., White M. F.,
941 Naismith J. H. (2016) Mechanism of DNA loading by the DNA repair helicase XPD.
942 *Nucleic Acids Res* **44:** 2806-2815

943 Danev R., Baumeister W. (2017) Expanding the boundaries of cryo-EM with
944 phase plates. *Curr Opin Struct Biol* **46:** 87-94

945 Devault A., Martinez A. M., Fesquet D., Labbé J. C., Morin N., Tassan J. P., Nigg E. A.,
946 Cavadore J. C., Dorée M. (1995) MAT1 ('menage à trois') a new RING finger
947 protein subunit stabilizing cyclin H-cdk7 complexes in starfish and Xenopus CAK.
948 *EMBO J* **14:** 5027-5036

949 Di Lello P., Jenkins L. M. M., Jones T. N., Nguyen B. D., Hara T., Yamaguchi H.,
950 Dikeakos J. D., Appella E., Legault P., Omichinski J. G. (2006) Structure of the
951 Tfb1/p53 complex: Insights into the interaction between the p62/Tfb1 subunit
952 of TFIIH and the activation domain of p53. *Mol Cell* **22:** 731-740

953 Di Lello P., Miller Jenkins L. M., Mas C., Langlois C., Malitskaya E., Fradet-Turcotte
954 A., Archambault J., Legault P., Omichinski J. G. (2008) p53 and TFIIEalpha share a
955 common binding site on the Tfb1/p62 subunit of TFIIH. *Proc Natl Acad Sci USA*
956 **105:** 106-111

957 Drapkin R., Le Roy G., Cho H., Akoulitchev S., Reinberg D. (1996) Human cyclin-
958 dependent kinase-activating kinase exists in three distinct complexes. *Proc Natl*
959 *Acad Sci USA* **93:** 6488-6493

960 Dubaele S., Proietti De Santis L., Bienstock R. J., Keriel A., Stefanini M., Van Houten
961 B., Egly J.-M. (2003) Basal transcription defect discriminates between xeroderma
962 pigmentosum and trichothiodystrophy in XPD patients. *Mol Cell* **11:** 1635-1646

963 Emsley P., Lohkamp B., Scott W. G., Cowtan K. (2010) Features and development
964 of Coot. *Acta Crystallogr D Biol Crystallogr* **66:** 486-501

965 Evans E., Moggs J. G., Hwang J. R., Egly J. M., Wood R. D. (1997) Mechanism of
966 open complex and dual incision formation by human nucleotide excision repair
967 factors. *EMBO J* **16:** 6559-6573

968 Fairman-Williams M. E., Guenther U.-P., Jankowsky E. (2010) SF1 and SF2
969 helicases: family matters. *Curr Opin Struct Biol* **20:** 313-324

970 Fan L., Arvai A. S., Cooper P. K., Iwai S., Hanaoka F., Tainer J. A. (2006) Conserved
971 XPB core structure and motifs for DNA unwinding: implications for pathway
972 selection of transcription or excision repair. *Mol Cell* **22:** 27-37

973 Fan L., Fuss J. O., Cheng Q. J., Arvai A. S., Hammel M., Roberts V. A., Cooper P. K.,
974 Tainer J. A. (2008) XPD helicase structures and activities: insights into the cancer
975 and aging phenotypes from XPD mutations. *Cell* **133:** 789-800

976 Fishburn J., Tomko E., Galburt E., Hahn S. (2015) Double-stranded DNA
977 translocase activity of transcription factor TFIIH and the mechanism of RNA
978 polymerase II open complex formation. *Proc Natl Acad Sci USA* **112:** 3961-3966

979 Fisher R. P., Jin P., Chamberlin H. M., Morgan D. O. (1995) Alternative
980 mechanisms of CAK assembly require an assembly factor or an activating kinase.
981 *Cell* **83:** 47-57

982 Fisher R. P., Morgan D. O. (1994) A novel cyclin associates with MO15/CDK7 to
983 form the CDK-activating kinase. *Cell* **78:** 713-724

984 Fregoso M., Lainé J.-P., Aguilar-Fuentes J., Mocquet V., Reynaud E., Coin F., Egly J.-
985 M., Zurita M. (2007) DNA repair and transcriptional deficiencies caused by
986 mutations in the Drosophila p52 subunit of TFIIH generate developmental
987 defects and chromosome fragility. *Mol Cell Biol* **27:** 3640-3650

988 Gervais V., Busso D., Wasielewski E., Poterszman A., Egly J. M., Thierry J. C.,
989 Kieffer B. (2001) Solution structure of the N-terminal domain of the human
990 TFIIH MAT1 subunit: new insights into the RING finger family. *J Biol Chem* **276:**
991 7457-7464

992 Gervais V., Lamour V., Jawhari A., Frindel F., Wasielewski E., Dubaele S., Egly J.-M.,
993 Thierry J.-C., Kieffer B., Poterszman A. (2004) TFIIH contains a PH domain
994 involved in DNA nucleotide excision repair. *Nat Struct Mol Biol* **11:** 616-622

995 Gibbons B. J., Brignole E. J., Azubel M., Murakami K., Voss N. R., Bushnell D. A.,
996 Asturias F. J., Kornberg R. D. (2012) Subunit architecture of general transcription
997 factor TFIIH. *Proc Natl Acad Sci USA* **109:** 1949-1954

998 Giglia-Mari G., Coin F., Ranish J. A., Hoogstraten D., Theil A., Wijgers N., Jaspers N.
999 G. J., Raams A., Argentini M., van der Spek P. J. et al (2004) A new, tenth subunit of
1000 TFIIH is responsible for the DNA repair syndrome trichothiodystrophy group A.
1001 *Nat Genet* **36:** 714-719

1002 Greber B. J., Nguyen T. H. D., Fang J., Afonine P. V., Adams P. D., Nogales E. (2017)
1003 The cryo-electron microscopy structure of human transcription factor IIH.
1004 *Nature* **549:** 414-417

1005 Grünberg S., Warfield L., Hahn S. (2012) Architecture of the RNA polymerase II
1006 preinitiation complex and mechanism of ATP-dependent promoter opening. *Nat*
1007 *Struct Mol Biol* **19:** 788-796

1008 Guzder S. N., Qiu H., Sommers C. H., Sung P., Prakash L., Prakash S. (1994) DNA
1009 repair gene RAD3 of S. cerevisiae is essential for transcription by RNA
1010 polymerase II. *Nature* **367:** 91-94

1011 He Y., Fang J., Taatjes D. J., Nogales E. (2013) Structural visualization of key steps
1012 in human transcription initiation. *Nature* **495:** 481-486

1013 He Y., Yan C., Fang J., Inouye C., Tjian R., Ivanov I., Nogales E. (2016) Near-atomic
1014 resolution visualization of human transcription promoter opening. *Nature* **533:**
1015 359-365

1016 Headd J. J., Echols N., Afonine P. V., Grosse-Kunstleve R. W., Chen V. B., Moriarty
1017 N. W., Richardson D. C., Richardson J. S., Adams P. D. (2012) Use of knowledge-
1018 based restraints in phenix.refine to improve macromolecular refinement at low
1019 resolution. *Acta Crystallogr D Biol Crystallogr* **68:** 381-390

1020 Herrera-Moyano E., Moriel-Carretero M., Montelone B. A., Aguilera A. (2014) The
1021 rem mutations in the ATP-binding groove of the Rad3/XPD helicase lead to
1022 Xeroderma pigmentosum-Cockayne syndrome-like phenotypes. *PLoS Genet* **10:**
1023 e1004859

1024 Hilario E., Li Y., Nobumori Y., Liu X., Fan L. (2013) Structure of the C-terminal half
1025 of human XPB helicase and the impact of the disease-causing mutation XP11BE.
1026 *Acta Crystallogr D Biol Crystallogr* **69:** 237-246

1027 Huang J. C., Svoboda D. L., Reardon J. T., Sancar A. (1992) Human nucleotide
1028 excision nuclease removes thymine dimers from DNA by incising the 22nd
1029 phosphodiester bond 5' and the 6th phosphodiester bond 3' to the photodimer.
1030 *Proc Natl Acad Sci USA* **89:** 3664-3668

1031 Jawhari A., Boussert S., Lamour V., Atkinson R. A., Kieffer B., Poch O., Potier N.,
1032 Van Dorsselaer A., Moras D., Poterszman A. (2004) Domain architecture of the
1033 p62 subunit from the human transcription/repair factor TFIIH deduced by

1034 limited proteolysis and mass spectrometry analysis. *Biochemistry* **43:** 14420-
1035 14430

1036 Jawhari A., Lainé J.-P., Dubaele S., Lamour V., Poterszman A., Coin F., Moras D.,
1037 Egly J.-M. (2002) p52 Mediates XPB function within the transcription/repair
1038 factor TFIIH. *J Biol Chem* **277:** 31761-31767

1039 Jones T. A., Zou J. Y., Cowan S. W., Kjeldgaard M. (1991) Improved methods for
1040 building protein models in electron density maps and the location of errors in
1041 these models. *Acta Crystallogr A Found Crystallogr* **47 (Pt. 2):** 110-119

1042 Kainov D. E., Vitorino M., Cavarelli J., Poterszman A., Egly J.-M. (2008) Structural
1043 basis for group A trichothiodystrophy. *Nat Struct Mol Biol* **15:** 980-984

1044 Kelley L. A., Mezulis S., Yates C. M., Wass M. N., Sternberg M. J. E. (2015) The
1045 Phyre2 web portal for protein modeling, prediction and analysis. *Nat Protoc* **10:**
1046 845-858

1047 Khoshouei M., Radjainia M., Baumeister W., Danev R. (2017) Cryo-EM structure
1048 of haemoglobin at 3.2 Å determined with the Volta phase plate. *Nat Commun* **8:**
1049 16099

1050 Kim J. S., Saint-André C., Lim H. S., Hwang C.-S., Egly J.-M., Cho Y. (2015) Crystal
1051 structure of the Rad3/XPD regulatory domain of Ssl1/p44. *J Biol Chem* **290:**
1052 8321-8330

1053 Kimanius D., Forsberg B. O., Scheres S. H., Lindahl E. (2016) Accelerated cryo-EM
1054 structure determination with parallelisation using GPUs in RELION-2. *Elife* **5:**
1055 e18722

1056 Kralund H. H., Ousager L., Jaspers N. G., Raams A., Pedersen E. B., Gade E., Bygum
1057 A. (2013) Xeroderma Pigmentosum-Trichothiodystrophy overlap patient with
1058 novel XPD/ERCC2 mutation. *Rare Dis* **1:** e24932

1059 Krissinel E., Henrick K. (2007) Inference of macromolecular assemblies from
1060 crystalline state. *J Mol Biol* **372:** 774-797

1061 Kuper J., Braun C., Elias A., Michels G., Sauer F., Schmitt D. R., Poterszman A., Egly
1062 J.-M., Kisker C. (2014) In TFIIH, XPD helicase is exclusively devoted to DNA
1063 repair. *PLoS Biol* **12:** e1001954

1064 Kuper J., Wolski S. C., Michels G., Kisker C. (2012) Functional and structural
1065 studies of the nucleotide excision repair helicase XPD suggest a polarity for DNA
1066 translocation. *EMBO J* **31:** 494-502

1067 Lafrance-Vanasse J., Arseneault G., Cappadocia L., Legault P., Omichinski J. G.
1068 (2013) Structural and functional evidence that Rad4 competes with Rad2 for
1069 binding to the Tfb1 subunit of TFIIH in NER. *Nucleic Acids Res* **41:** 2736-2745

1070 Li C.-L., Golebiowski F. M., Onishi Y., Samara N. L., Sugasawa K., Yang W. (2015)
1071 Tripartite DNA Lesion Recognition and Verification by XPC, TFIIH, and XPA in
1072 Nucleotide Excision Repair. *Mol Cell* **59:** 1025-1034

1073 Liu H., Rudolf J., Johnson K. A., McMahon S. A., Oke M., Carter L., McRobbie A.-M.,
1074 Brown S. E., Naismith J. H., White M. F. (2008) Structure of the DNA Repair
1075 Helicase XPD. *Cell* **133:** 801-812

1076 Liu J., Huang C., Shin D.-H., Yokota H., Jancarik J., Kim J.-S., Adams P. D., Kim R.,
1077 Kim S.-H. (2005) Crystal structure of a heat-inducible transcriptional repressor
1078 HrcA from Thermotoga maritima: structural insight into DNA binding and
1079 dimerization. *J Mol Biol* **350:** 987-996

1080 Luo J., Cimermančič P., Viswanath S., Ebmeier C. C., Kim B., Dehecq M., Raman V.,
1081 Greenberg C. H., Pellarin R., Sali A. et al (2015) Architecture of the Human and
1082 Yeast General Transcription and DNA Repair Factor TFIIH. *Mol Cell* **59:** 794-806

1083 Mason A. C., Rambo R. P., Greer B., Pritchett M., Tainer J. A., Cortez D., Eichman B.
1084 F. (2014) A structure-specific nucleic acid-binding domain conserved among
1085 DNA repair proteins. *Proc Natl Acad Sci USA* **111:** 7618-7623

1086 Mathieu N., Kaczmarek N., Rüthemann P., Luch A., Naegeli H. (2013) DNA quality
1087 control by a lesion sensor pocket of the xeroderma pigmentosum group D
1088 helicase subunit of TFIIH. *Curr Biol* **23:** 204-212

1089 Mlak R., Krawczyk P., Homa-Mlak I., Powrózek T., Ciesielka M., Kozioł P.,
1090 Milanowski J., Małecka-Massalska T. (2018) Predictive Value of Single Nucleotide
1091 Polymorphisms of ERCC1, XPA, XPC, XPD and XPG Genes, Involved in NER
1092 Mechanism in Patients with Advanced NSCLC Treated with Cisplatin and
1093 Gemcitabine. *Pathol Oncol Res***:** 1-11

1094 Moriel-Carretero M., Aguilera A. (2010) A postincision-deficient TFIIH causes
1095 replication fork breakage and uncovers alternative Rad51- or Pol32-mediated
1096 restart mechanisms. *Mol Cell* **37:** 690-701

1097 Moriel-Carretero M., Herrera-Moyano E., Aguilera A. (2015) A unified model for
1098 the molecular basis of Xeroderma pigmentosum-Cockayne Syndrome. *Rare Dis* **3:**
1099 e1079362

1100 Murakami K., Tsai K.-L., Kalisman N., Bushnell D. A., Asturias F. J., Kornberg R. D.
1101 (2015) Structure of an RNA polymerase II preinitiation complex. *Proc Natl Acad*
1102 *Sci USA* **112:** 13543-13548

1103 Naegeli H., Bardwell L., Friedberg E. C. (1993) Inhibition of Rad3 DNA helicase
1104 activity by DNA adducts and abasic sites: implications for the role of a DNA
1105 helicase in damage-specific incision of DNA. *Biochemistry* **32:** 613-621

1106 Nakane T., Kimanius D., Lindahl E., Scheres S. H. (2018) Characterisation of
1107 molecular motions in cryo-EM single-particle data by multi-body refinement in
1108 RELION. *Elife* **7:** e36861

1109 Nguyen T. H. D., Galej W. P., Bai X.-C., Oubridge C., Newman A. J., Scheres S. H. W.,
1110 Nagai K. (2016) Cryo-EM structure of the yeast U4/U6.U5 tri-snRNP at 3.7 Å
1111 resolution. *Nature* **530:** 298-302

1112 Nguyen T. H. D., Galej W. P., Bai X.-C., Savva C. G., Newman A. J., Scheres S. H. W.,
1113 Nagai K. (2015) The architecture of the spliceosomal U4/U6.U5 tri-snRNP.
1114 *Nature* **523:** 47-52

1115 Nguyen T. H. D., Li J., Galej W. P., Oshikane H., Newman A. J., Nagai K. (2013)
1116 Structural basis of Brr2-Prp8 interactions and implications for U5 snRNP
1117 biogenesis and the spliceosome active site. *Structure* **21:** 910-919

1118 Obmolova G., Ban C., Hsieh P., Yang W. (2000) Crystal structures of mismatch
1119 repair protein MutS and its complex with a substrate DNA. *Nature* **407:** 703-710

1120 Oksenych V., Bernardes de Jesus B., Zhovmer A., Egly J.-M., Coin F. (2009)
1121 Molecular insights into the recruitment of TFIIH to sites of DNA damage. *EMBO J*
1122 **28:** 2971-2980

1123 Okuda M., Nakazawa Y., Guo C., Ogi T., Nishimura Y. (2017) Common TFIIH
1124 recruitment mechanism in global genome and transcription-coupled repair
1125 subpathways. *Nucleic Acids Res* **45:** 13043-13055

1126 Peters G. J., Avan A., Ruiz M. G., Orsini V., Avan A., Giovannetti E., Smit E. F. (2014)
1127 Predictive role of repair enzymes in the efficacy of Cisplatin combinations in
1128 pancreatic and lung cancer. *Anticancer Res* **34:** 435-442

1129 Pettersen E. F., Goddard T. D., Huang C. C., Couch G. S., Greenblatt D. M., Meng E.
1130 C., Ferrin T. E. (2004) UCSF Chimera--a visualization system for exploratory
1131 research and analysis. *J Comput Chem* **25:** 1605-1612

1132 Poterszman A., Lamour V., Egly J. M., Moras D., Thierry J. C., Poch O. (1997) A
1133 eukaryotic XPB/ERCC3-like helicase in Mycobacterium leprae? *Trends Biochem*
1134 *Sci* **22:** 418-419

1135 Radu L., Schoenwetter E., Braun C., Marcoux J., Koelmel W., Schmitt D. R., Kuper J.,
1136 Cianférani S., Egly J. M., Poterszman A. et al (2017) The intricate network
1137 between the p34 and p44 subunits is central to the activity of the
1138 transcription/DNA repair factor TFIIH. *Nucleic Acids Res* **45:** 10872-10883

1139 Rapin I. (2013) Disorders of nucleotide excision repair. *Handb Clin Neurol* **113:**
1140 1637-1650

1141 Riou L., Zeng L., Chevallier-Lagente O., Stary A., Nikaido O., Taïeb A., Weeda G.,
1142 Mezzina M., Sarasin A. (1999) The relative expression of mutated XPB genes
1143 results in xeroderma pigmentosum/Cockayne's syndrome or
1144 trichothiodystrophy cellular phenotypes. *Hum Mol Genet* **8:** 1125-1133

1145 Robert X., Gouet P. (2014) Deciphering key features in protein structures with
1146 the new ENDscript server. *Nucleic Acids Res* **42:** W320-324

1147 Robinson P. J., Trnka M. J., Bushnell D. A., Davis R. E., Mattei P.-J., Burlingame A. L.,
1148 Kornberg R. D. (2016) Structure of a Complete Mediator-RNA Polymerase II Pre-
1149 Initiation Complex. *Cell* **166:** 1411-1422.e1416

1150 Rosenthal P. B., Henderson R. (2003) Optimal determination of particle
1151 orientation, absolute hand, and contrast loss in single-particle electron
1152 cryomicroscopy. *J Mol Biol* **333:** 721-745

1153 Rossignol M., Kolb-Cheynel I., Egly J. M. (1997) Substrate specificity of the cdk-
1154 activating kinase (CAK) is altered upon association with TFIIH. *EMBO J* **16:** 1628-
1155 1637

1156 Rouillon C., White M. F. (2010) The XBP-Bax1 helicase-nuclease complex
1157 unwinds and cleaves DNA: implications for eukaryal and archaeal nucleotide
1158 excision repair. *J Biol Chem* **285:** 11013-11022

1159 Rudolf J., Makrantoni V., Ingledew W. J., Stark M. J. R., White M. F. (2006) The
1160 DNA repair helicases XPD and FancJ have essential iron-sulfur domains. *Mol Cell*
1161 **23:** 801-808

1162 Sainsbury S., Bernecky C., Cramer P. (2015) Structural basis of transcription
1163 initiation by RNA polymerase II. *Nat Rev Mol Cell Biol* **16:** 129-143

1164 Sandrock B., Egly J. M. (2001) A yeast four-hybrid system identifies Cdk-
1165 activating kinase as a regulator of the XPD helicase, a subunit of transcription
1166 factor IIH. *J Biol Chem* **276:** 35328-35333

1167 Scheres S. H. W. (2010) Classification of Structural Heterogeneity by Maximum-
1168 Likelihood Methods. *Meth Enz* **482:** 295-320

1169 Scheres S. H. W. (2012) RELION: implementation of a Bayesian approach to cryo-
1170 EM structure determination. *J Struct Biol* **180:** 519-530

1171 Scheres S. H. W. (2015) Semi-automated selection of cryo-EM particles in
1172 RELION-1.3. *J Struct Biol* **189:** 114-122

1173 Scheres S. H. W., Chen S. (2012) Prevention of overfitting in cryo-EM structure
1174 determination. *Nat Meth* **9:** 853-854

1175 Schilbach S., Hantsche M., Tegunov D., Dienemann C., Wigge C., Urlaub H., Cramer
1176 P. (2017) Structures of transcription pre-initiation complex with TFIIH and
1177 Mediator. *Nature* **551:** 204-209

1178 Seroz T., Perez C., Bergmann E., Bradsher J., Egly J. M. (2000) p44/SSL1, the
1179 regulatory subunit of the XPD/RAD3 helicase, plays a crucial role in the
1180 transcriptional activity of TFIIH. *J Biol Chem* **275:** 33260-33266

1181 Shiekhattar R., Mermelstein F., Fisher R. P., Drapkin R., Dynlacht B., Wessling H.
1182 C., Morgan D. O., Reinberg D. (1995) Cdk-activating kinase complex is a
1183 component of human transcription factor TFIIH. *Nature* **374:** 283-287

1184 Sugasawa K., Akagi J.-i., Nishi R., Iwai S., Hanaoka F. (2009) Two-step recognition
1185 of DNA damage for mammalian nucleotide excision repair: Directional binding of
1186 the XPC complex and DNA strand scanning. *Mol Cell* **36:** 642-653

1187 Sugitani N., Sivley R. M., Perry K. E., Capra J. A., Chazin W. J. (2016) XPA: A key
1188 scaffold for human nucleotide excision repair. *DNA Repair (Amst)* **44:** 123-135

1189 Svejstrup J. Q., Wang Z., Feaver W. J., Wu X., Bushnell D. A., Donahue T. F.,
1190 Friedberg E. C., Kornberg R. D. (1995) Different forms of TFIIH for transcription
1191 and DNA repair: holo-TFIIH and a nucleotide excision repairosome. *Cell* **80:** 21-
1192 28

1193 Theron T., Fousteri M. I., Volker M., Harries L. W., Botta E., Stefanini M., Fujimoto
1194 M., Andressoo J.-O., Mitchell J., Jaspers N. G. J. et al (2005) Transcription-
1195 associated breaks in xeroderma pigmentosum group D cells from patients with
1196 combined features of xeroderma pigmentosum and Cockayne syndrome. *Mol Cell*
1197 *Biol* **25:** 8368-8378

1198 Tirode F., Busso D., Coin F., Egly J. M. (1999) Reconstitution of the transcription
1199 factor TFIIH: assignment of functions for the three enzymatic subunits, XPB, XPD,
1200 and cdk7. *Mol Cell* **3:** 87-95

1201 Tremeau-Bravard A., Perez C., Egly J. M. (2001) A role of the C-terminal part of
1202 p44 in the promoter escape activity of transcription factor IIH. *J Biol Chem* **276:**
1203 27693-27697

1204 Tsai K.-L., Yu X., Gopalan S., Chao T.-C., Zhang Y., Florens L., Washburn M. P.,
1205 Murakami K., Conaway R. C., Conaway J. W. et al (2017) Mediator structure and
1206 rearrangements required for holoenzyme formation. *Nature Publishing Group***:** 1-
1207 19

1208 Vermeulen W., Rademakers S., Jaspers N. G., Appeldoorn E., Raams A., Klein B.,
1209 Kleijer W. J., Hansen L. K., Hoeijmakers J. H. (2001) A temperature-sensitive
1210 disorder in basal transcription and DNA repair in humans. *Nat Genet* **27:** 299-
1211 303

1212 Vitorino M., Coin F., Zlobinskaya O., Atkinson R. A., Moras D., Egly J.-M.,
1213 Poterszman A., Kieffer B. (2007) Solution structure and self-association
1214 properties of the p8 TFIIH subunit responsible for trichothiodystrophy. *J Mol Biol*
1215 **368:** 473-480

1216 Warfield L., Luo J., Ranish J., Hahn S. (2016) Function of conserved topological
1217 regions within the S. cerevisiae basal transcription factor TFIIH. *Mol Cell Biol* **36:**
1218 2464-2475

1219 Winkler G. S., Araújo S. J., Fiedler U., Vermeulen W., Coin F., Egly J. M.,
1220 Hoeijmakers J. H., Wood R. D., Timmers H. T., Weeda G. (2000) TFIIH with
1221 inactive XPD helicase functions in transcription initiation but is defective in DNA
1222 repair. *J Biol Chem* **275:** 4258-4266

1223 Wirth N., Gross J., Roth H. M., Buechner C. N., Kisker C., Tessmer I. (2016)
1224 Conservation and Divergence in Nucleotide Excision Repair Lesion Recognition. *J*
1225 *Biol Chem* **291:** 18932-18946

1226 Wolski S. C., Kuper J., Hänzelmann P., Truglio J. J., Croteau D. L., Van Houten B.,
1227 Kisker C. (2008) Crystal structure of the FeS cluster-containing nucleotide
1228 excision repair helicase XPD. *PLoS Biol* **6:** e149

1229 Zhang K. (2016) Gctf: Real-time CTF determination and correction. *J Struct Biol*
1230 **193:** 1-12

1231 Zheng S. Q., Palovcak E., Armache J.-P., Verba K. A., Cheng Y., Agard D. A. (2017)
1232 MotionCor2: anisotropic correction of beam-induced motion for improved cryo-
1233 electron microscopy. *Nat Meth* **14:** 331-332

1234 Ziani S., Nagy Z., Alekseev S., Soutoglou E., Egly J.-M., Coin F. (2014) Sequential
1235 and ordered assembly of a large DNA repair complex on undamaged chromatin. *J*
1236 *Cell Biol* **206:** 589-598
1237

1238

1239

1240 **Figure supplements**

1241

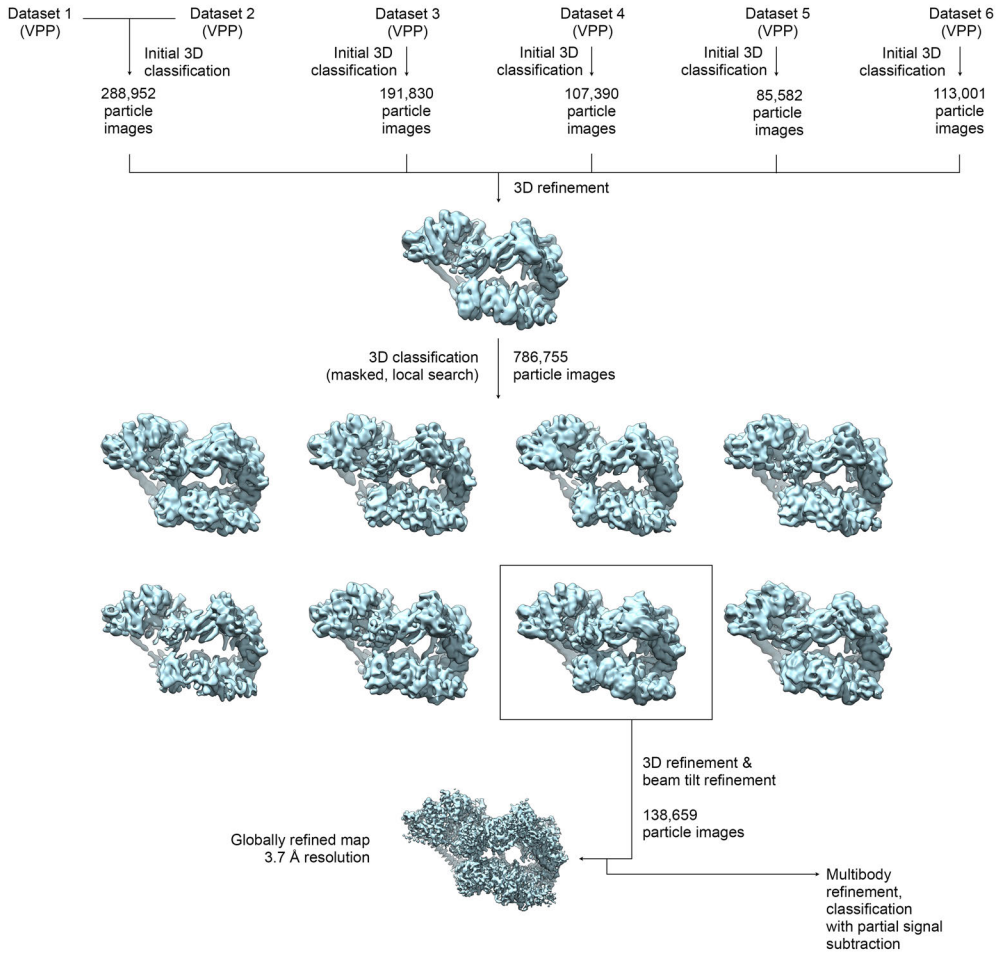

1242

1243 **Figure 1 - figure supplement 1. Data processing scheme for global**
1244 **reconstruction.** The datasets (DS) were initially processed individually, with the
1245 exception of DS6, where particles from DS4 were used to compensate for
1246 orientation bias, and DS1/DS2, which were joined for processing. Subsequently,
1247 the datasets were pooled and sub-classified. The best class of was used for the
1248 final refinement to obtain a globally refined map at 3.7 Å resolution (see Figure 1
1249 – figure supplement 2). The classified VPP dataset was also used for further
1250 processing and classification of sub-regions (Figure 1 – figure supplements 3-5).

1251

1252

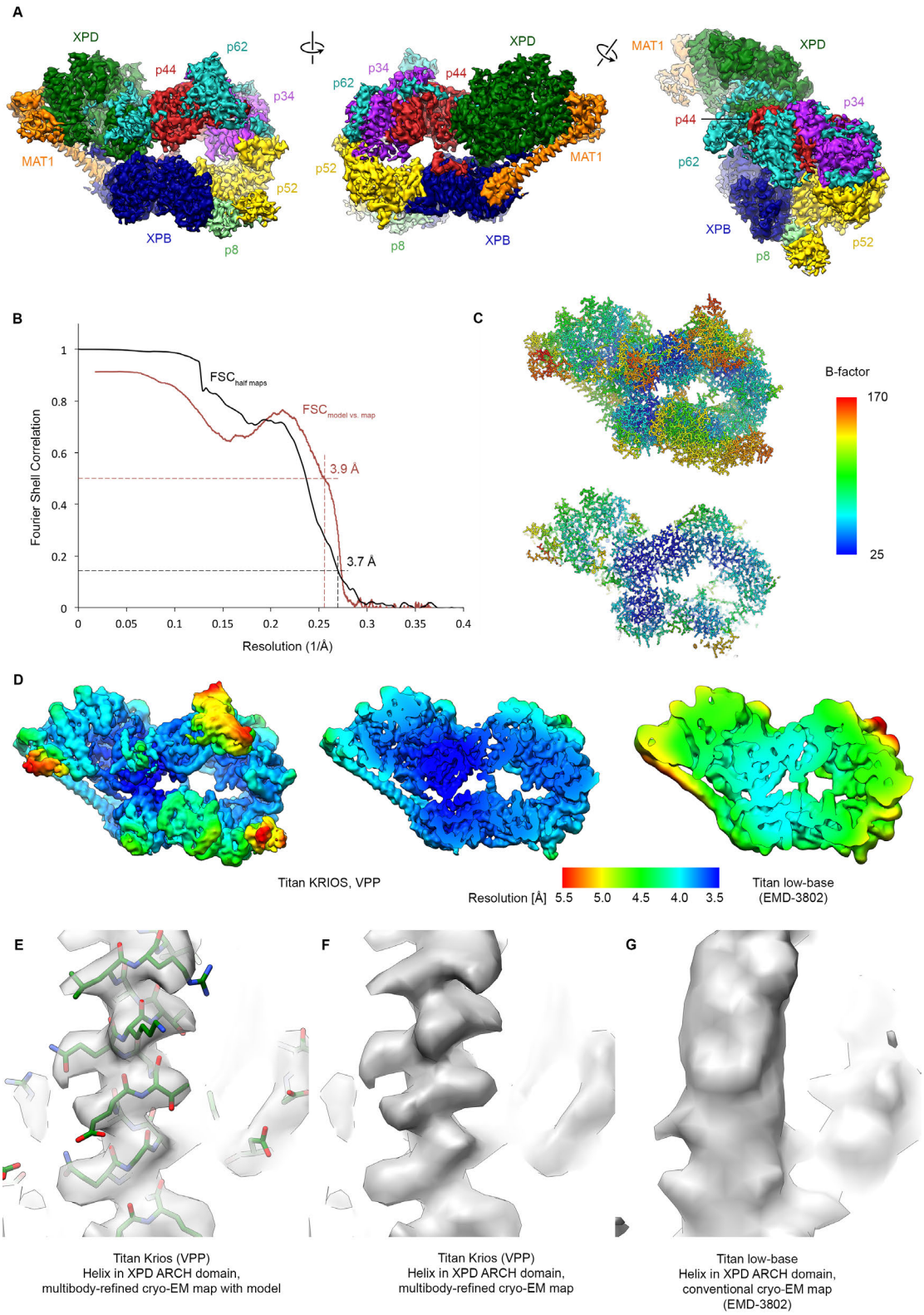

Figure 1 – figure supplement 2. Resolution estimation, validation statistics, and quality of the density. (**A**) Three views of the refined, sharpened, and low-pass filtered cryo-EM map of the TFIIH core complex. Protein subunits are color-coded and labeled. (**B**) Fourier shell correlation (FSC) curves. Black: FSC curve

between half-maps. Red: FSC curve between map and refined model. The resolution at the appropriate thresholds (Rosenthal & Henderson, 2003; Scheres & Chen, 2012) is indicated. (**C**) B-factor distribution on the refined TFIIH coordinate model. (**D**) Local resolution estimation, computed by windowed FSC in RELION 2. (**E**, **F**, **G**) Comparison of the 3.6 Å multibody-refined cryo-EM map of the TFIIH core complex (E, F) with our previous 4.4 Å cryo-EM map (G) shows substantial improvements in map quality in the more peripheral and flexible regions of the complex (an α-helix from the XPD ARCH domain is shown).

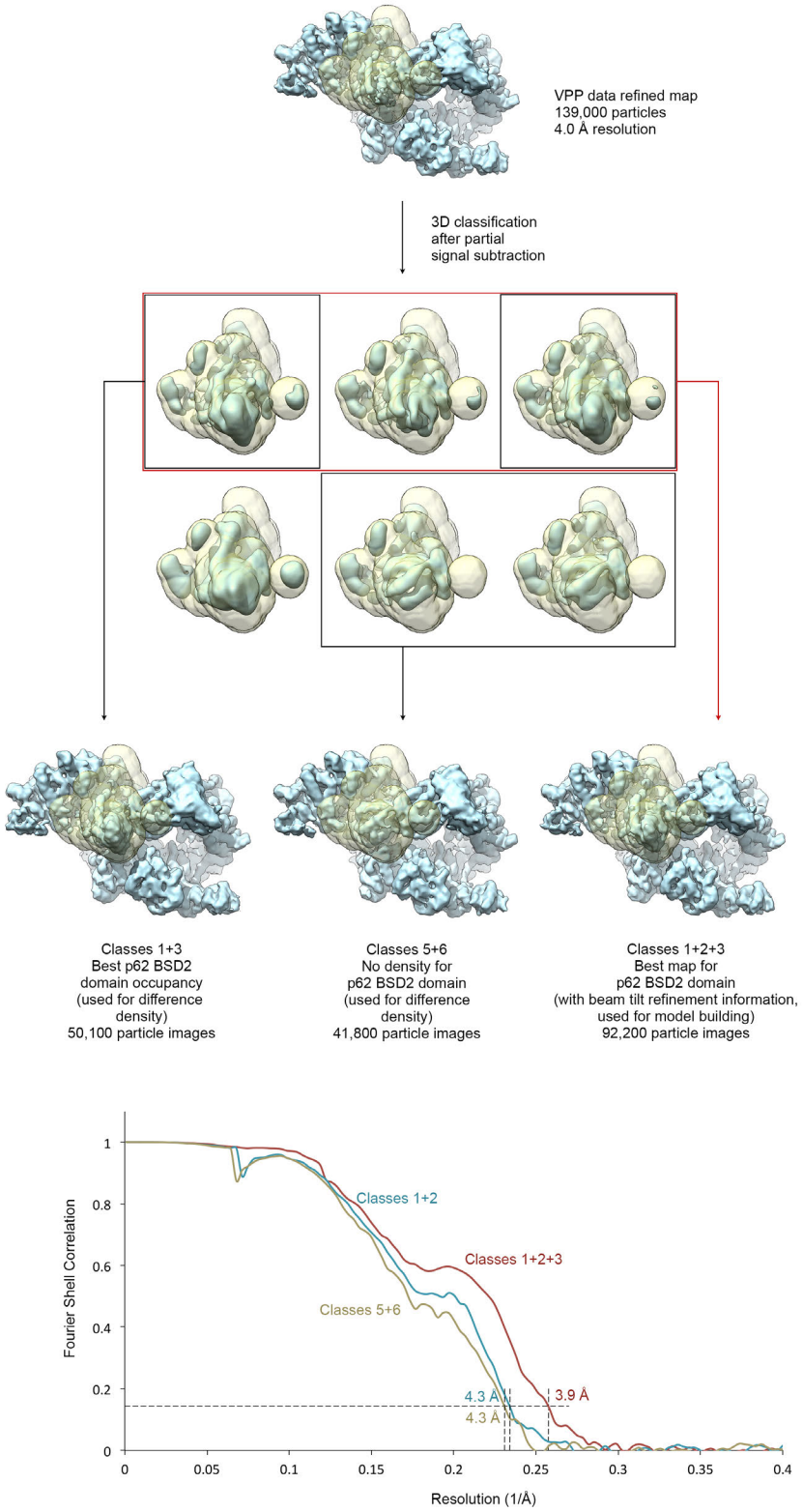

Figure 1 – figure supplement 3. Focused classification of the p62 BSD2 domain. (**A**) Focused classification for the p62 BSD2 domain and adjacent structural elements using the classified VPP dataset (indicated in Figure 1 –

figure supplement 1). Partial signal subtraction (Bai et al., 2015) and masking were used to focus the classification on the region of interest (mask shown in transparent yellow). Selected classes were refined using the selected but un-subtracted particle images because the region of interest is too small for efficient image alignment (Nguyen et al., 2016). (**B**) FSC curves for the three refined maps shown in (A), indicating resolution of 3.9-4.3 Å according to the FSC = 0.143 criterion (Rosenthal & Henderson, 2003).

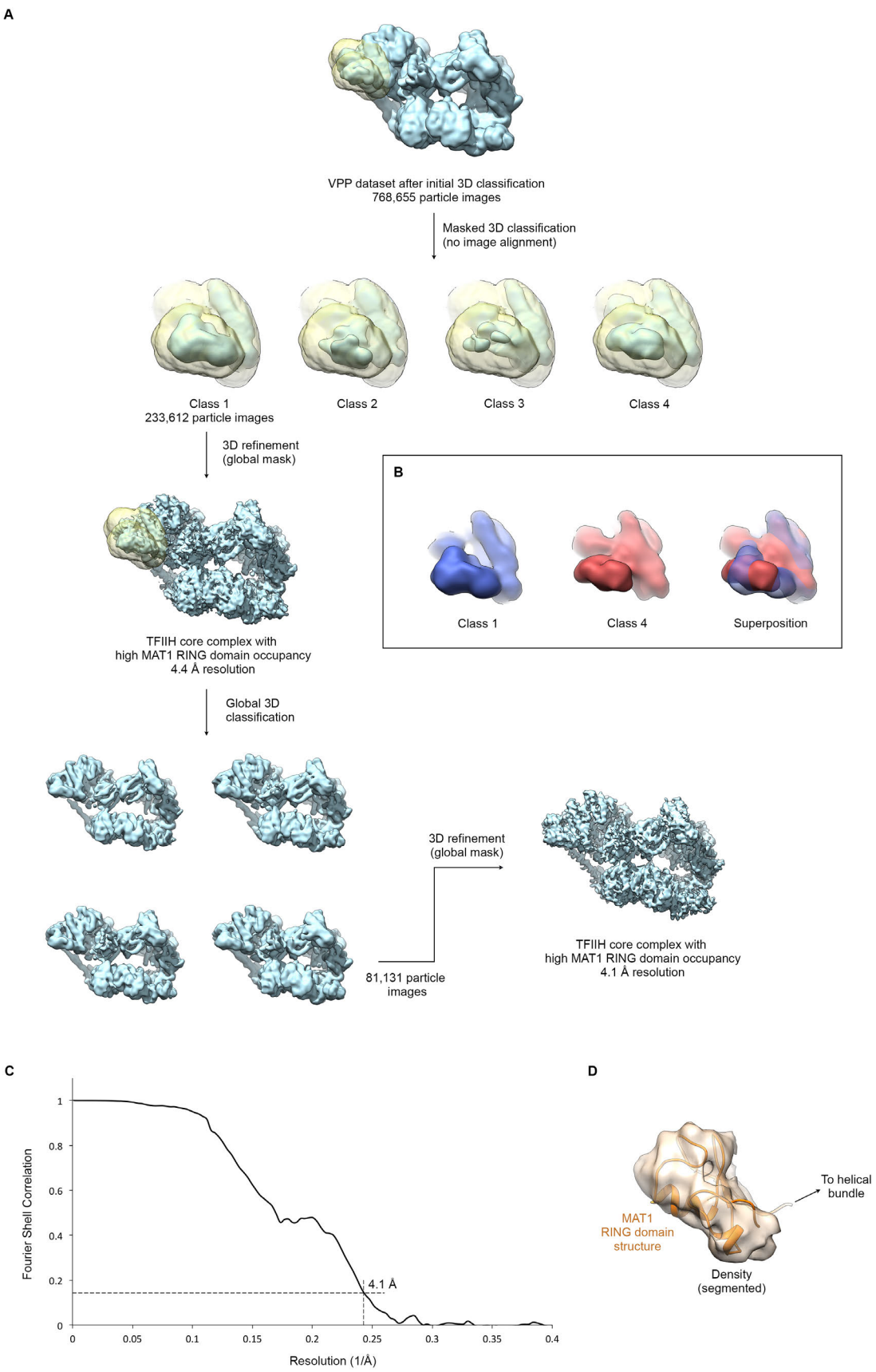

Figure 1 – figure supplement 4. Focused classification and interpretation of the MAT1 RING domain density. (**A**) The entire pool of pre-classified TFIIH

1284 particles from the VPP datasets was subjected to alignment-free focused 3D
1285 classification using a mask that covers the MAT1 RING domain and helical
1286 bundle. Signal subtraction was not required due to the peripheral location of the
1287 region in the complex and the orientation distribution of the particle images.
1288 After one round of additional global classification (to select for overall particle
1289 quality and conformation), the class showing the most highly occupied density
1290 for the MAT1 RING domain was refined to 4.1 Å resolution (using beam tilt
1291 values imported from the best-resolution refinement, Figure 1 – figure
1292 supplement 1). (**B**) 3D classes differed not only in occupancy (i.e. classes 2 and 3
1293 showed low occupancy and fragmented density for the MAT1 RING domain) but
1294 also in the orientation of the MAT1 RING domain, which is flexibly attached to
1295 the complex. Classes 1 and 4 are shown in different colors individually and
1296 superposed to highlight the different orientations of the MAT1 RING domain. (**C**)
1297 The FSC curve estimates a resolution of 4.1 Å for the refined map of TFIIH with
1298 high occupancy of the MAT1 RING domain. (**D**) Best fit of the structure of the
1299 MAT1 RING domain (Gervais et al., 2001) into the cryo-EM map, obtained using
1300 the FITMAP command in UCSF CHIMERA (Pettersen et al., 2004) with 100
1301 independent initial placements before local optimization at 5 Å resolution. This
1302 fit shows the best correlation between model and map and additionally satisfies
1303 geometrical constraints imposed by the continuity of the peptide chain between
1304 the RING domain and the MAT1 helical bundle.
1305

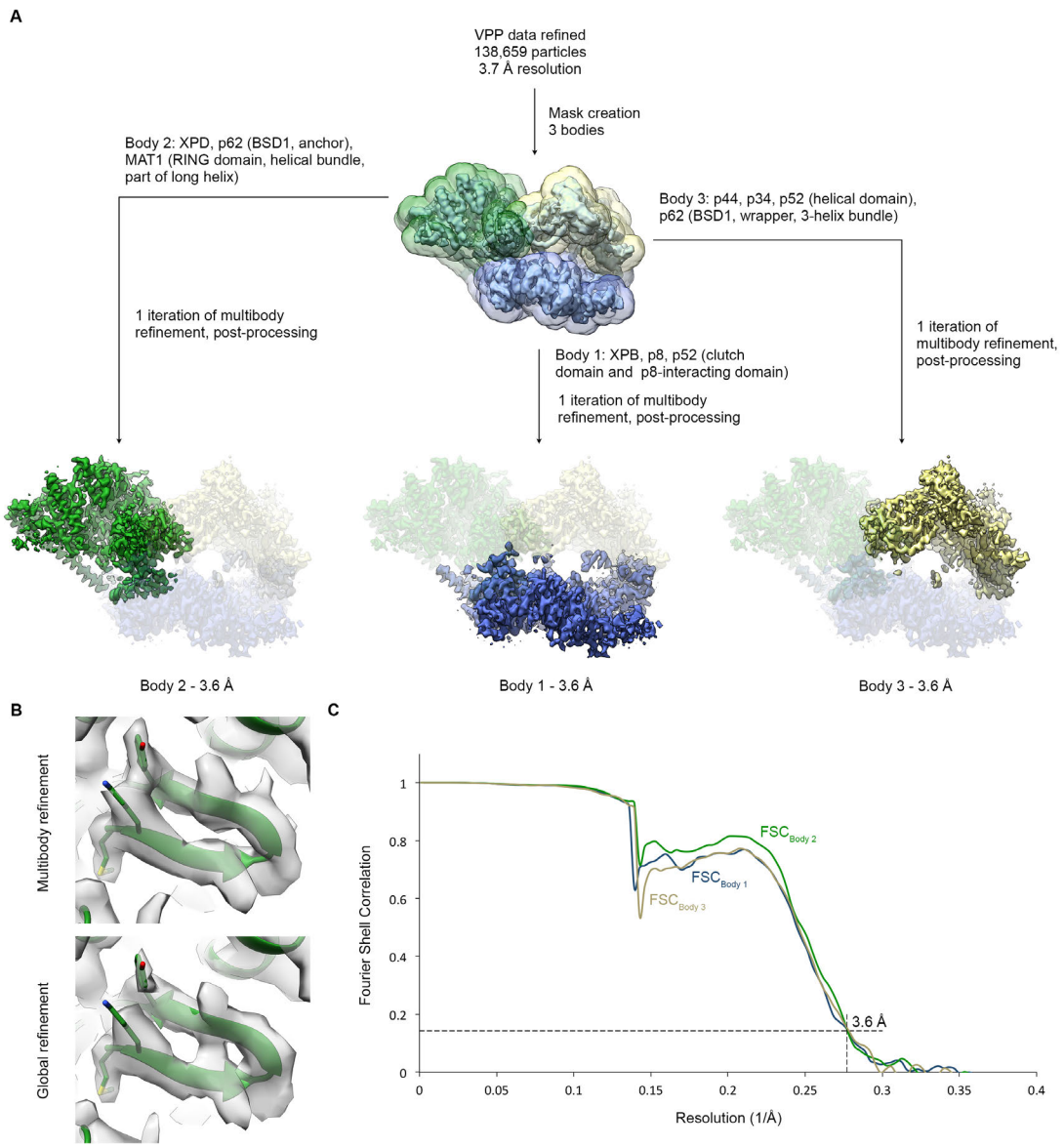

Figure 1 – figure supplement 5. Multibody refinement. (**A**) Schematic for multibody refinement (Nakane et al., 2018) of the classified VPP dataset (indicated in Figure 1 – figure supplement 1). Three bodies were used and subjected to multibody refinement using the corresponding masks. (**B**) Example of the improvement of the cryo-EM density for the XPD N-terminus after multibody refinement (top) relative to the global refinement (bottom). (**C**) FSC curves for the refined bodies, indicating resolutions of 3.6 Å according to the FSC = 0.143 criterion (Rosenthal & Henderson, 2003).

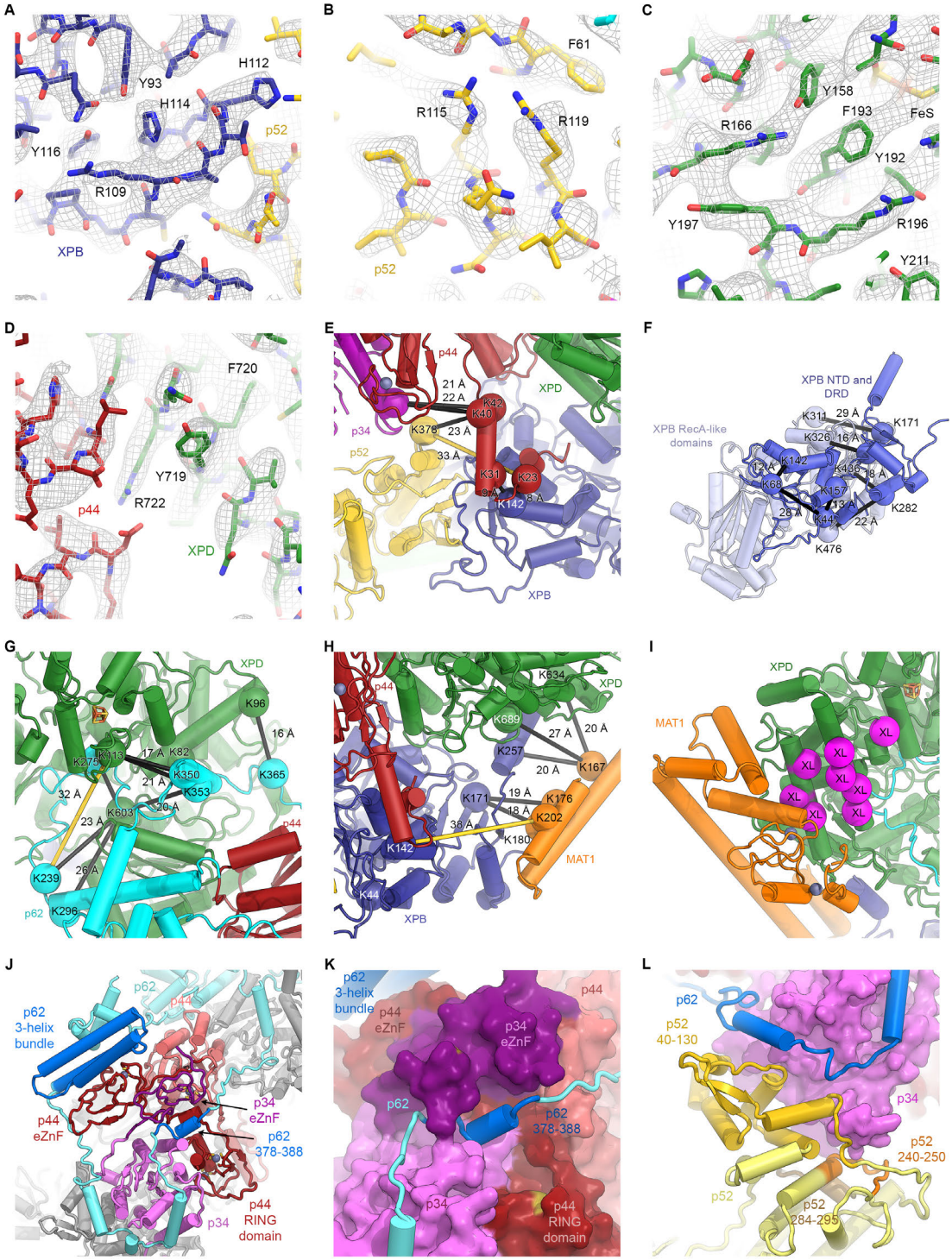

Figure 1 – figure supplement 6. Detailed architecture of the TFIIH core complex. (**A-D**) The refined coordinate model is shown in the 3.7 Å-resolution cryo-EM map. Large side chains are indicated. (**E-H**) Mapping of CX-MS data (Luo et al., 2015) onto the atomic coordinate model. Crosslinked residues are shown as spheres, crosslinks as black lines (crosslinks > 30 Å apart as yellow lines). (**E**) Crosslinks between the p44 NTE and XPB, p52, and p34 confirm the tracing of

1323 the p44 NTE towards the XPB NTD. (**F**) Intramolecular crosslinks in XPB validate
1324 the tracing of the XPB NTD. (**G**) Crosslinks between p62 and XPD. Crosslinks
1325 between p62 and p44 are not shown (see Methods and Supplementary Data
1326 Table 1). (**H**) Crosslinks between MAT1 and XPB and XPD. One strong outlier
1327 connecting XPB K44 to the MAT1 helical bundle (>100 Å distance) is a likely false
1328 positive and is not shown. (**I**) Location of site-specific crosslinks between RAD3,
1329 the yeast XPD homolog (RAD3 residues carrying the crosslinker mapped onto
1330 the XPD structure and shown as purple spheres) and TFB3, the yeast MAT1
1331 homolog (Warfield et al., 2016). (**J**) Interlocking zinc-binding domains of p44 and
1332 p34 mediate interactions between these proteins in the hinge region. The p62 C-
1333 terminal 3-helix bundle binds to the p44 eZnF domain. (**K**) Residues 378-388 of
1334 p62 are sandwiched between the zinc-binding domains of p34 and p44. (**L**) View
1335 of the p62-p52-p34 interaction region.
1336
1337

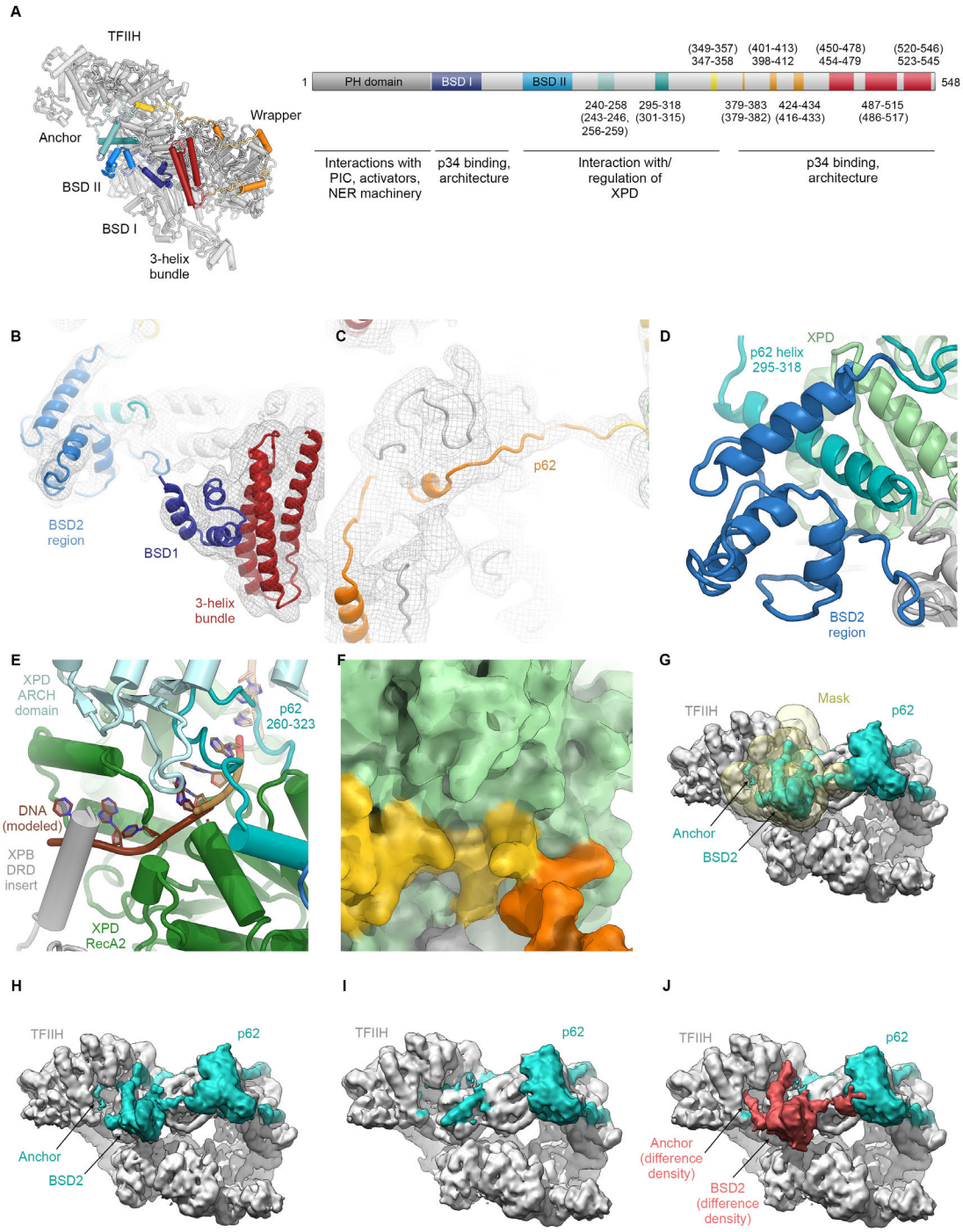

Figure 2 – figure supplement 1. Analysis of the structure of p62. (**A**) p62 architecture and sequence assignment. Fitting of domains (see **B**), secondary structure prediction for α-helices (Kelley et al., 2015), helical segments of the cryo-EM map, and density for large side chains were used for initial assignment of the trace of p62. The final model shows good agreement of observed helical segments (residue numbers indicated) and secondary structure prediction for α-

1345 helices (residue numbers given in brackets). (**B**) Fitting of p62 BSD1 (PDB ID
1346 2DII; blue) into the TFIIH cryo-EM map. Due to flexibility, the density in this
1347 region is weak and was low-pass filtered to 6 Å for interpretation and fitting. In
1348 agreement with previous results (Schilbach et al., 2017), this domain interacts
1349 with the p62 C-terminal three-helix bundle (purple), which in turn sits on the
1350 eZnF domain of p44 (Figure 1 – figure supplement 6J), thereby explaining the
1351 importance of the latter region for functional TFIIH (Tremeau-Bravard et al.,
1352 2001). (**C**) Extended segments of the p62 chain were interpreted using the low-
1353 pass filtered map as described in (B) to maintain continuity of the cryo-EM
1354 density. (**D**) The p62 helix 295-317 is sandwiched between the BSD2 region of
1355 p62 and XPD RecA2, thereby bridging these two elements of TFIIH. (**E**) XPD-
1356 bound DNA was modeled by domain-wise superposition of the structures of a
1357 XPD-DNA complex (Constantinescu-Aruxandei et al., 2016) and the structure of
1358 DNA-bound Hel308 (Büttner et al., 2007) onto TFIIH. The presence of the p62
1359 anchor near XPD RecA2 leads to steric hindrance with the DNA that would
1360 prevent binding. (**F**) Residues 346-361 of p62 block access to the XPD
1361 nucleotide-binding pocket. (**G-J**) Analysis of p62 (teal) conformational dynamics.
1362 (**G**) Particle images were sorted for p62 elements near XPD using signal-
1363 subtracted focused classification (mask shown in yellow; see Figure 1 – figure
1364 supplement 3). (**H**) Refined class with p62 density near XPD. (**I**) Refined class
1365 without p62 density near XPD. (**J**) Difference density (red) between the densities
1366 shown in H, I. Both classes show intact particles, even in the absence of the p62
1367 segment inserted into the XPD substrate binding cavity.
1368
1369

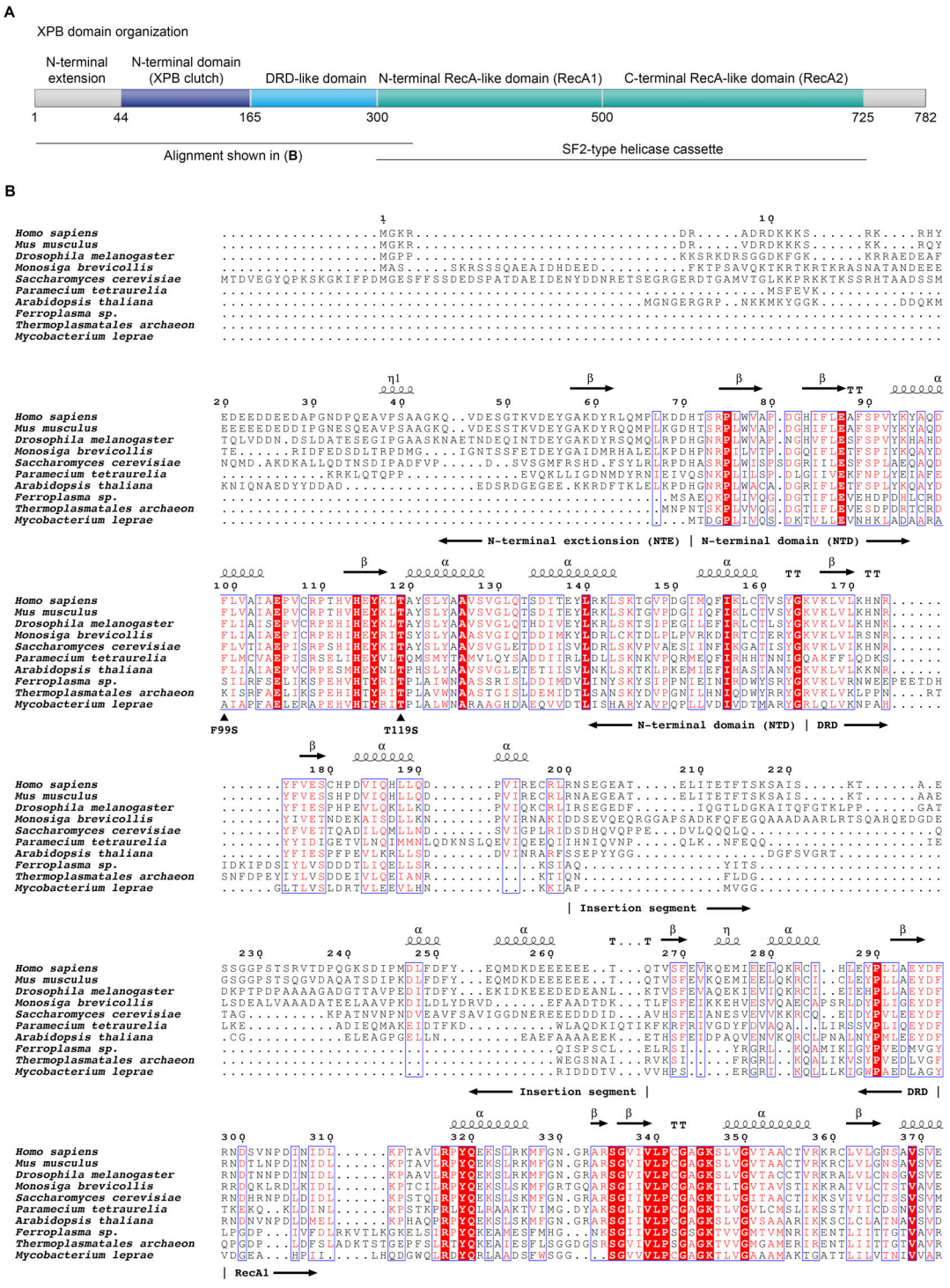

Figure 3 – figure supplement 1. Domain organization of XPB and sequence alignment of the N-terminal regions of XPB or XPB-like enzymes from eukaryotes, archaea, and bacteria. (**A**) Domain organization of human XPB, color-coded as in Figure 2C. (**B**) Sequence alignments. Sequences used (species and UNIPROT or GENBANK accession code indicated): Human (*Homo sapiens*, P19447), mouse (*Mus musculus*, P49135), fruit fly (*Drosophila melanogaster*, Q02870), Choanoflagellate (*Monosiga brevicollis*, A9V0A0), fungus

1378 (*Saccharomyces cerevisiae*, Q00578), ciliate (*Paramecium tetraurelia*,
1379 XP_001448651.1), plant (*Arabidopsis thaliana*, Q38861), archaea (*Ferroplasma*,
1380 EQB73227.1, *Thermoplasmatales*, EQB71900.1), bacteria (*Mycobacterium leprae*,
1381 Q9CBE0) (Balasingham et al., 2012; Poterszman et al., 1997). Some archaeal
1382 XPBs, including the *Archaeoglobus fulgidus* homolog that served for structure
1383 determination (Fan et al., 2006), contain only the DRD, lacking the NTD/NTE,
1384 and were not included. Residues are numbered according to the human
1385 sequence. Identical residues are printed white on red background, similar
1386 residues in red on white background. Secondary structure elements, residues
1387 mutated in human disease (F99S, T119S), and the approx. 70-residue insertion
1388 in the DRD are indicated. Figure generated using the ESPript web server (Robert
1389 & Gouet, 2014).
1390
1391
1392

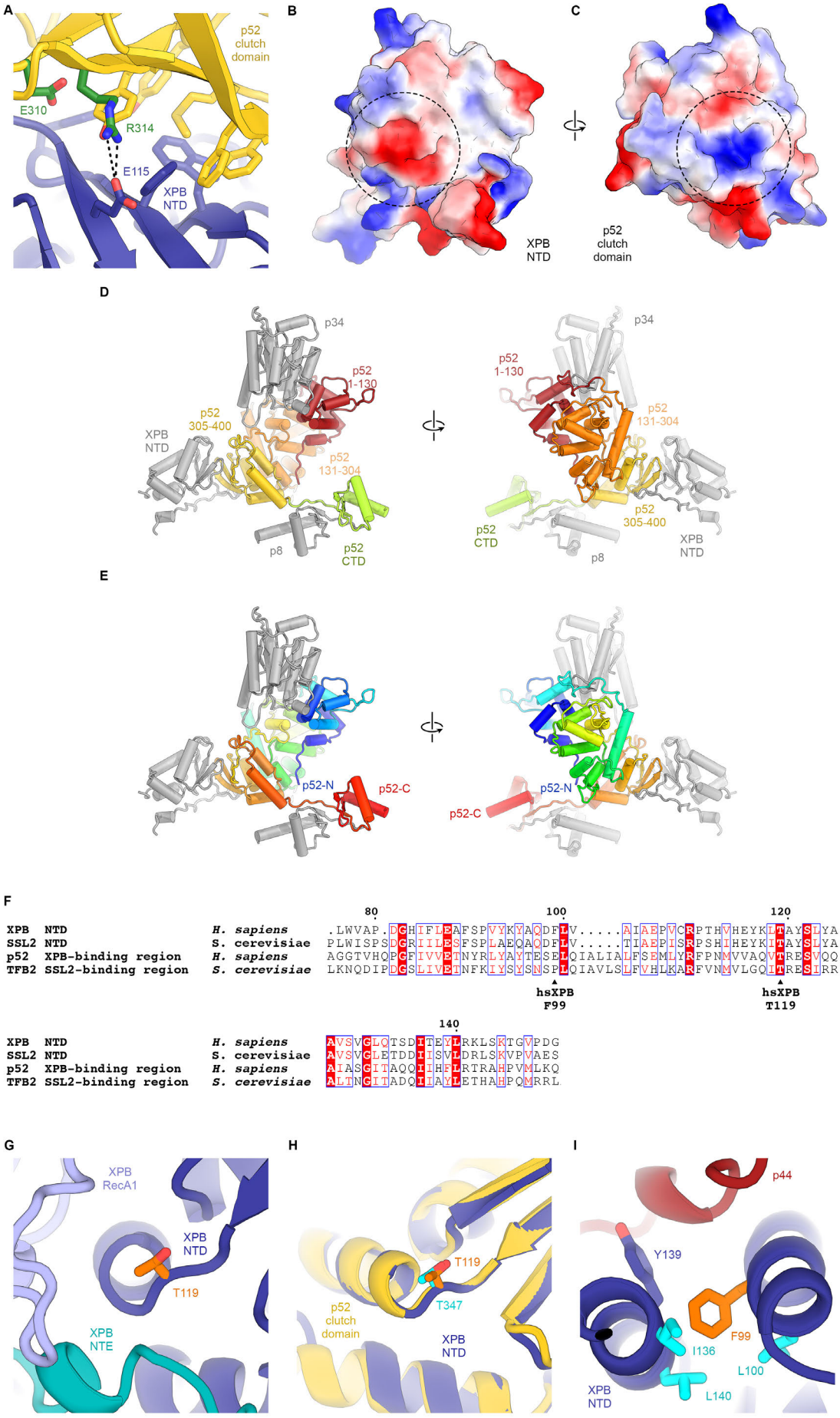
A
p52
clutch
domain
E310
R314
E115
XPB
NTD
B
XPB
NTD
C
p52
clutch
domain
D
p34
p52
1-130
p52
305-400
XPB
NTD
p52
131-304
p8
p52
CTD
p34
p52
1-130
p52
131-304
p52
305-400
p52
CTD
p8
XPB
NTD
E
p52-N
p52-C
p52-N
p52-C
F
80
100
120
XPB NTD H. sapiens .LWVAP.DGHIFLEAFSPVYKYAQDFLV.....AIAEPVCRPTHVHEYKLTAYSLYA
SSL2 NTD S. cerevisiae PLWISPSDGRIILESFSPLAEQAQDFLV.....TIAEPISRPSHIHEYKITAYSLYA
p52 XPB-binding region H. sapiens AGGTVHQPGFIVVETNYRLYAYTESELQIALIALFSEMLYRFPNMVVAQVTRESVQQ
TFB2 SSL2-binding region S. cerevisiae LKNQDIPDGSLIVETNFKIYSYSNSPLQIAVLSLFVHLKARFVNMVLGQITRESIRR
hsXPB
F99
hsXPB
T119
140
XPB NTD H. sapiens AVSVGLQTSDITEYLRKLSKTGVPDG
SSL2 NTD S. cerevisiae AVSVGLETDDIISVLDRLSKVPVAES
p52 XPB-binding region H. sapiens AIASGITAQQIIHFLRTRAHPVMLKQ
TFB2 SSL2-binding region S. cerevisiae ALTNGITADQIIAYLETHAHPQMRRL
G
XPB
RecA1
XPB
NTD
T119
XPB
NTE
H
T119
T347
p52
clutch
domain
XPB
NTD
I
p44
Y139
F99
I136
L100
L140
XPB
NTD

1393

1394 **Figure 3 – figure supplement 2. Structure and interactions of the XPB DRD**
1395 **and NTD.** (**A**) Interface between the XPB NTD and the p52-clutch domains.
1396 Contacts include several large hydrophobic residues, as well as a salt bridge
1397 between p52 R314 and XPB E115 (shown as sticks). Mutations of residues
1398 equivalent to R314 and E310 in *D. melanogaster* p52 lead to disease-like
1399 phenotypes (Fregoso et al., 2007). (**B**, **C**) Electrostatic surface potential of the
1400 interacting surfaces of the XPB NTD (**B**) and the p52 clutch domain (**C**) show
1401 charge complementarity (strongest complementary charge peak indicated by a
1402 circle). (**D**) Front and back views of the domain organization of p52. Residues 1-
1403 130 (red) and 131-304 (orange) are not in contact with the XPB NTD. Residues
1404 304-400 of p52 form the p52 clutch. Protein subunits or domains interacting
1405 with p52 are shown in grey. (**E**) Same as **D**, but p52 is colored using a gradient
1406 from blue (N-terminus) to red (C-terminus). (**F**) Sequence alignment of human
1407 and yeast p52 clutch and XPB NT domains highlights several highly conserved
1408 residues, including XPB T119, which is affected by a human disease mutation.
1409 Generated using the ESPript web server (Robert & Gouet, 2014). (**G**) Location of
1410 XPB T119, affected by the TTD mutation T119P, at a junction between a β-strand
1411 and an α-helix near the interface between XPB NTD, NTE, and RecA1 domains.
1412 (**H**) Superposition of the XPB NTD and the p52 clutch shows that a threonine at
1413 the position of XPB T119 also occurs in the p52 clutch. (**I**) The XP/CS mutation
1414 F99S affects a XPB NTD residue (orange) situated in a hydrophobic pocket
1415 formed by aliphatic residues (cyan) that are conserved across yeast and human
1416 XPB and p52 (**F**).
1417
1418

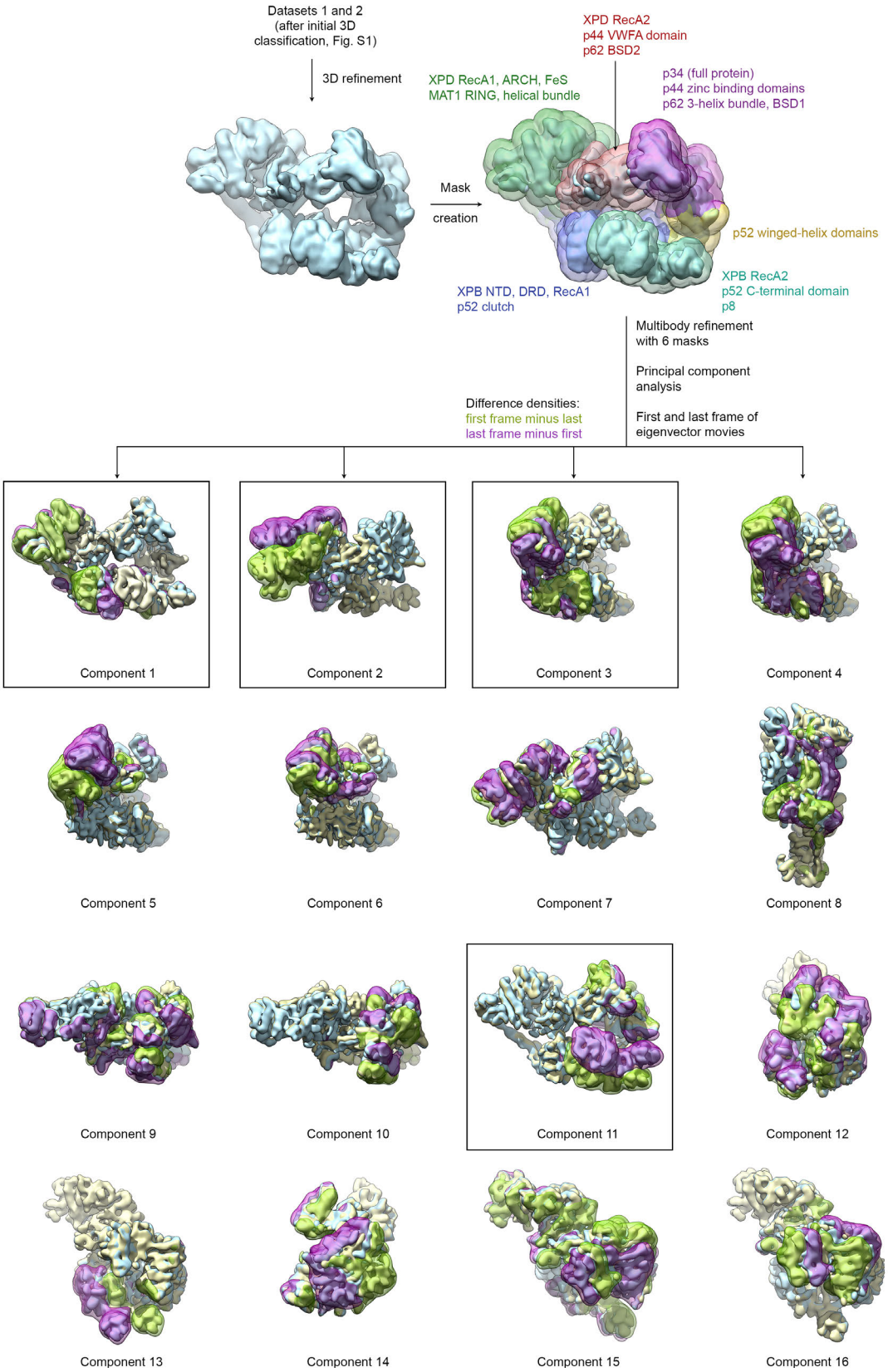

Figure 4 – figure supplement 1. Analysis of conformational variance of TFIIH. VPP datasets 1 and 2 were refined and subjected to multibody refinement using 6 masks followed by principal component analysis. The first and last

frames of the resulting eigenvector movies of the first 16 principal components are shown (in light blue and light yellow), along with difference densities obtained by subtracting the last volume from the first (green) and vice versa (purple). For the boxed components, the particles with the highest and lowest eigenvalues were extracted and refined (see Figure 4A).

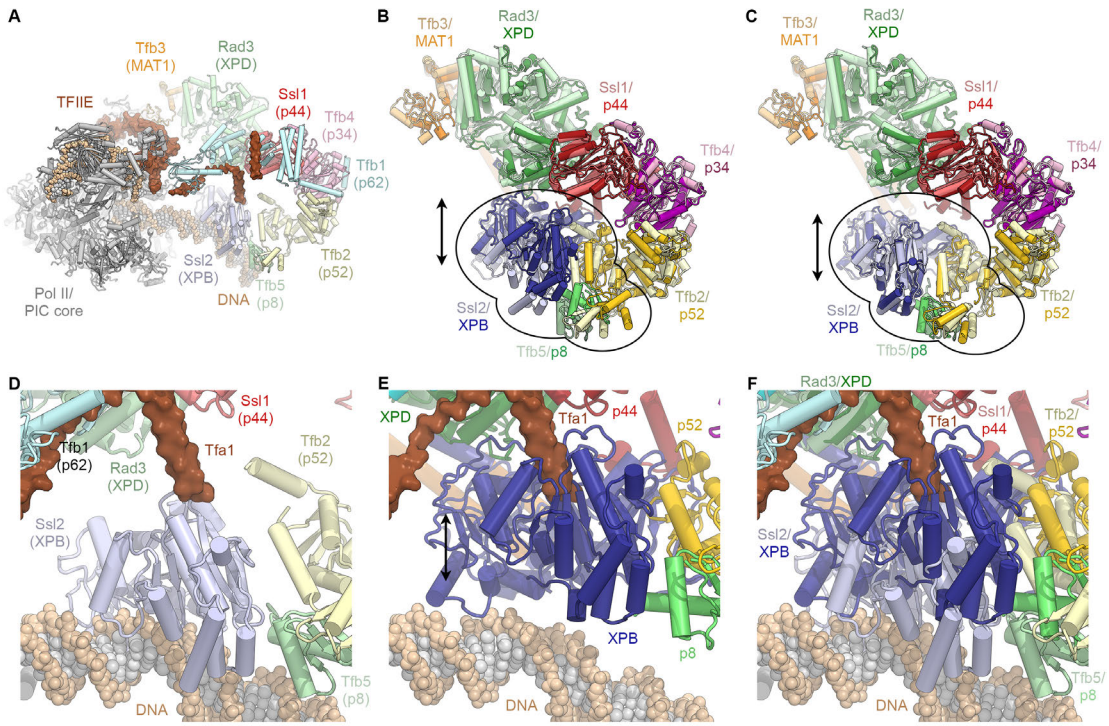

Figure 4 – figure supplement 2. Conformational dynamics of TFIIH and comparison with the PIC-bound TFIIH. (**A**) Rendering of the yeast TFIIH-containing Pol II-PIC (Schilbach et al., 2017). TFIIH subunits are colored and labeled with their yeast names, with human names in brackets. (**B**) Superposition of TFIIH from the yeast PIC (as shown in A, light colors) (Schilbach et al., 2017) and the complete structure of the human TFIIH core complex (this work; superposed on p44, bright colors) as single bodies. The top lobe of TFIIH (MAT1 helical bundle, XPB, p44, p34, p52 winged-helix domains; p62 not shown for clarity) aligns well, while the XPB-p52 (clutch/C-terminal domain)-p8 module is in a different position for the free and PIC-bound TFIIH (indicated). (**C**) Same as **B**, but with the human XPB-p52 (clutch/C-terminal domain)-p8 module superposed on the yeast structure as a rigid body. (**D**) View of DNA-bound Ssl2 (XPB) and neighboring subunits in the yeast Pol II-PIC (Schilbach et al., 2017). (**E**) View of human XPB, superposed on the yeast structure as in **B**. XPB could not bind DNA in this conformation, and the Tfa1 (TFIIE α-subunit) bridge helix, as observed in the yeast Pol II-PIC, clashes with XPB. (**F**) Panels **D** and **E** combined, visualizing the conformational change of TFIIH upon entry into the Pol II-PIC.

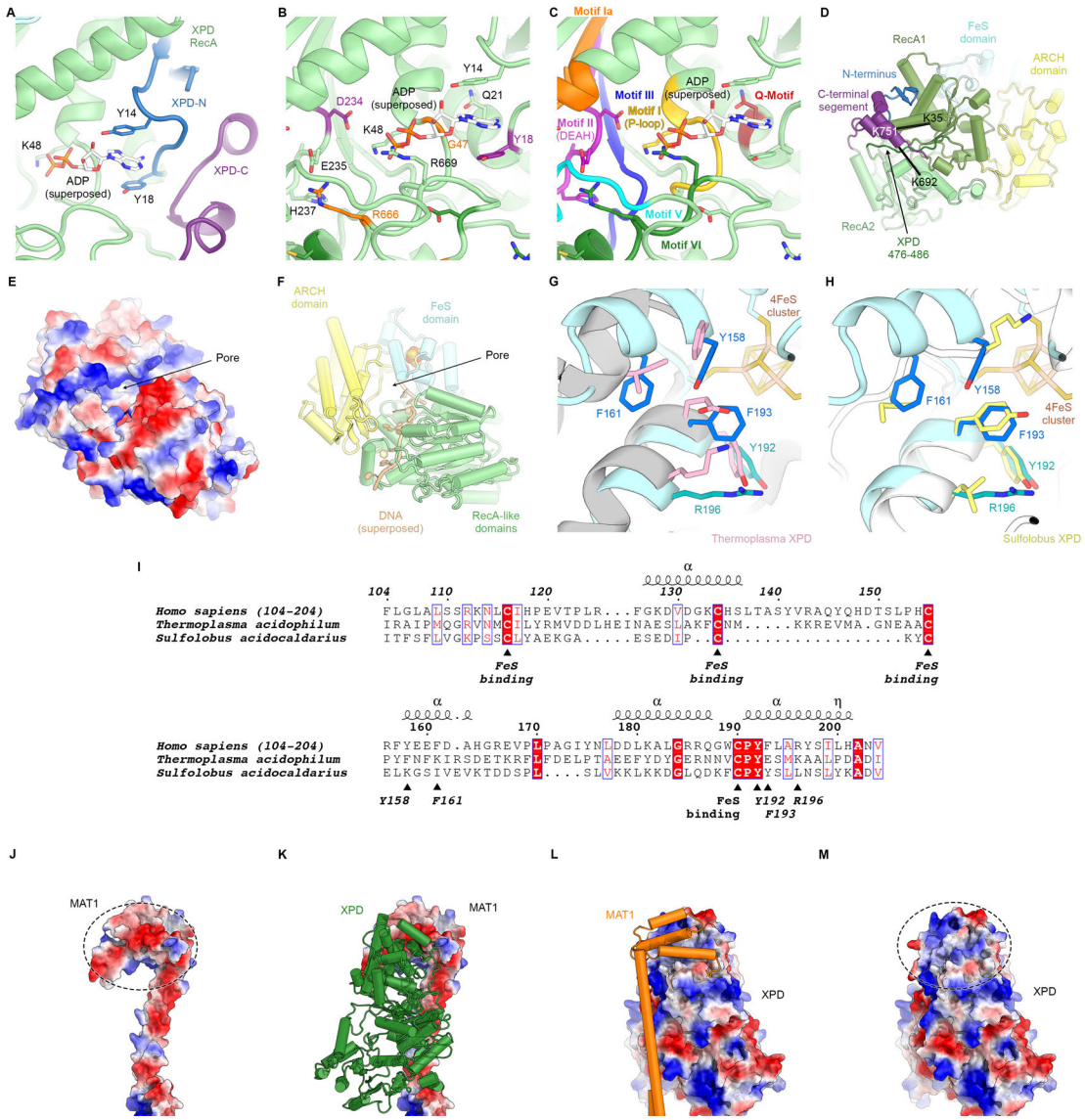

Figure 5 – figure supplement 1. Structure of XPD. (**A**) Close-up view of the XPD N- and C-terminal segments near the nucleotide binding pocket of the enzyme. Y12 and Y18 may stabilize nucleotides when bound (not present in our structure). (**B**) View of the nucleotide binding site of XPD with superposed ADP from PDB ID 4BGD (Nguyen et al., 2013). Residues mutated in human disease are shown as sticks and colored (purple: XP, orange: XP/CS, dark green, TTD). These include Y18, which we propose could form a stacking interaction with the base of a bound nucleotide, as well as residues in conserved helicase motifs (see **C**). (**C**) Same view as **B**, but with conserved helicase motifs color-coded. Motifs Q, I, II, and IV are involved in nucleotide binding and hydrolysis. (**D**) View of the back side of XPD, with the N- and C-terminal segments indicated. The C-terminal segment interacts with the linker between XPD RecA1 and RecA2 (residues 476-

1463 486). CX-MS crosslinks support the assignment of the C-terminal segment. The
1464 K751Q polymorphism has been associated with cancer therapy outcomes (Mlak
1465 et al., 2018; Peters et al., 2014), though functional differences between the
1466 variants has been debated (Clarkson & Wood, 2005). (**E**, **F**) Electrostatic surface
1467 (E) and cartoon (F) representations of the XPD structure, highlighting the pore
1468 between the XPD ARCH an FeS domains through which DNA (superposed from
1469 PDB IDs 5H8W, 2P6R (Büttner et al., 2007; Constantinescu-Aruxandei et al.,
1470 2016)) passes while being translocated by XPD. (**G**, **H**) Comparison of the
1471 structures of the human and archaeal FeS domains (**F**, *Thermoplasma*, PDB ID
1472 4A15 (Kuper et al., 2012), **G**, *Sulfolobus*, PDB ID 3CRV (Fan et al., 2008)). There
1473 are differences at the secondary structure level, and functionally important
1474 residues are only partially conserved. (**I**) Sequence alignment of FeS domains
1475 from human, *Sulfolobus*, and *Thermoplasma* XPD. With the exception of the
1476 conserved cysteine residues that bind the FeS-cluster, sequence conservation in
1477 this domain is relatively low. Residues discussed in the text are indicated. (**J**-**M**)
1478 Charge complementary of regions of negative and positive electrostatic potential
1479 near the MAT1 3-helix bundle and the XPD ARCH domain interface (circled).
1480
1481

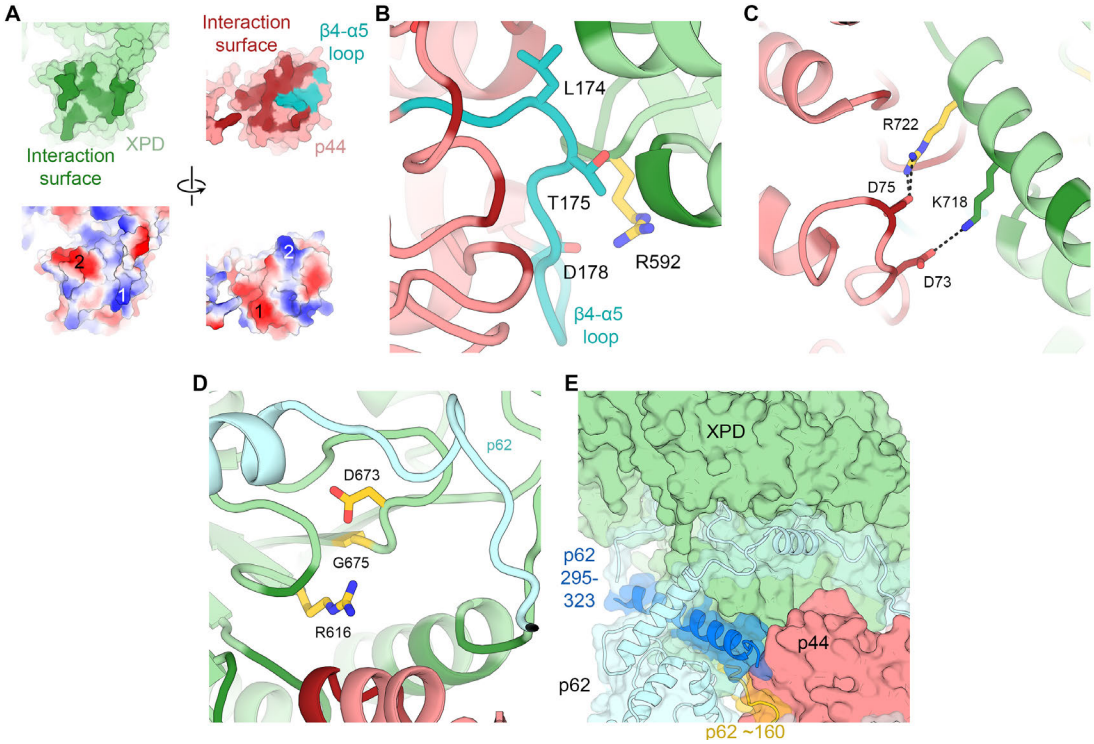

Figure 5 – figure supplement 2. XPD-p44 interaction. (**A**) Top: XPD-p44 (XPD green, p44 red) interaction surfaces are shown in darker shade (interacting residues in p44 β4-α5 loop are shown in teal). Bottom: Charge complementarity of the interface (two major complementary regions numbered 1 and 2). (**B**) Detailed view of the β4-α5 loop (teal) with mutations discussed in the text. XPD-p44 interacting regions (defined as residues within < 4 Å of neighboring protein) are colored in dark green (XPD) and dark red (p44). Residues discussed in the text are shown as sticks; those with mutation data (natural variants or experimental constructs) are colored yellow on XPD, teal on p44. (**C**) Detailed view of the interactions formed by XPD R722, which is mutated in TTD. (**D**) View of XPD residues R616, D673, and G675 in the context of p62 and p44. (**E**) XPD-p44-p62 interaction region. p62 segments interacting with both XPD and p44 are colored dark blue and yellow.

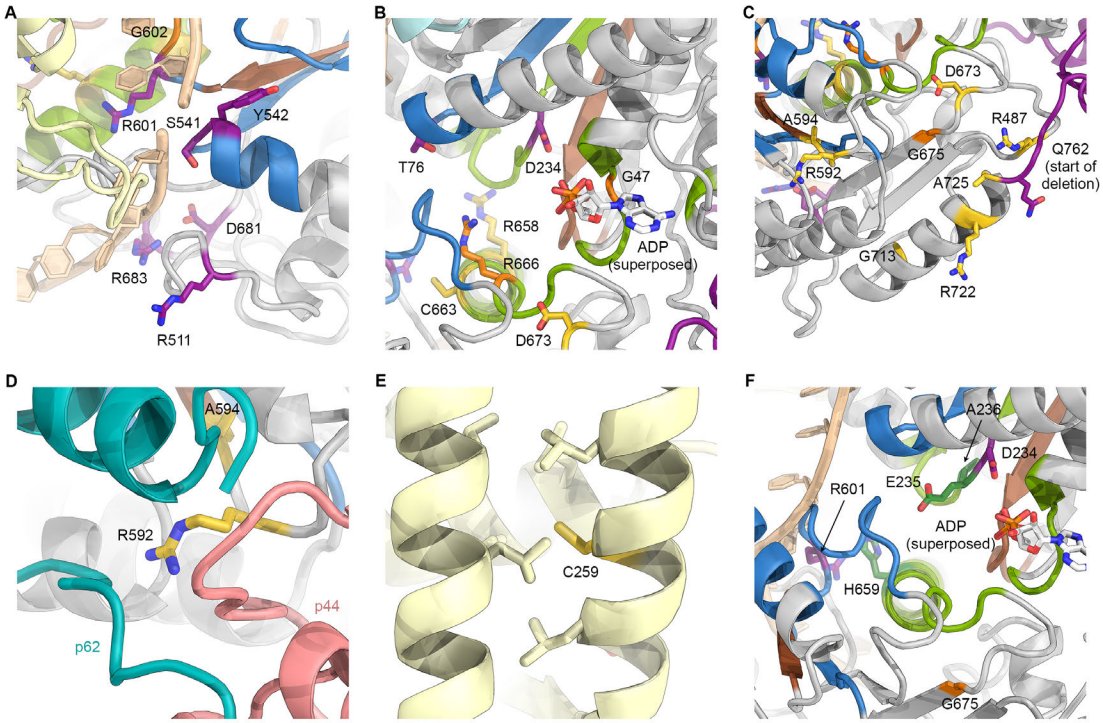

Figure 6 – figure supplement 1. Mapping of XPD disease mutations on the TFIIH structure. (**A**) Several residues affected by XP mutations localize near the DNA binding surfaces of XPD. This figure uses the same color scheme as Figure 6 (XP mutations purple; TTD yellow; CS-XP orange; helicase elements for DNA binding in blue, nucleotide binding and hydrolysis in green, coupling of nucleotide hydrolysis to DNA translocation in brown; DNA superposed from (Büttner et al., 2007)). (**B**) Mapping of mutations near the catalytic site of XPD. (**C**) Mutations near the interface with p44. Note the predominance of TTD mutations in this peripheral region of XPD. Also see Figure 5E, Figure 5 – figure supplement 2, and text for details. (**D**) XPD R592, affected by a TTD mutation is in a key location where p44, p62, and XPD interact. (**E**) Location of C259, affected by the C259Y mutation, which likely causes disruption of ARCH domain integrity and leads to defects in CAK subcomplex recruitment. (**F**) Mapping of yeast Rad3 *rem* mutations (green) onto our XPD structure. E235 and A236 are part of the conserved DEAH sequence motif (helicase motif II), as is the immediately adjacent XP mutation D234. H659 localizes near DNA (according to the superposed model) and may be involved in ordering R601, which is in direct contact with the modeled DNA and affected by an XP mutation.

Supplementary Information

for

The complete structure of the human TFIIH core complex

Basil J. Greber, Daniel B. Toso, Jie Fang, Eva Nogales*

* Correspondence should be addressed to E.N. (ENogales@lbl.gov).

This PDF files includes:

Supplementary Tables 1-3
Supplementary Notes 1-2

Other Supplementary Information for this manuscript includes the following:

Supplementary Data Table S1

1549

1550 **Supplementary Table 1. Data collection statistics.** All datasets were acquired
1551 on Gatan K2 Summit direct electron detectors mounted in 300 kV-electron
1552 microscopes with three-condenser type electron optics. Abbreviations: TEM,
1553 transmission electron microscope; VPP, volta phase plate; Σ, sum.

Data set #	TEM	VPP	Pixel size (Å)	Total dose ($e^-/Å^2$)	Frames	K2 acquisition mode	Total movies	Movies retained	Particles after initial 3D sorting	Particles in final map	Data reported
1	Titan KRIOS	Yes	1.15	50	33	Super-resolution	3,270	2,047	154,298	27,165	This study
2	Titan KRIOS	Yes	1.15	50	33	Super-resolution	3,190	1,804	134,654	23,034	This study
3	Titan KRIOS	Yes	1.15	50	33	Super-resolution	4,804	3,269	191,830	18,365	This study
4	Titan KRIOS	Yes	1.15	50	33	Super-resolution	3,283	2,709	107,390	32,008	This study
5	Titan KRIOS	Yes	1.15	50	33	Super-resolution	4,958	2,857	85,582	22,717	This study
6	Titan KRIOS	Yes	1.15	50	50	Super-resolution	1,932	1,631	113,001	15,370	This study
7	Titan KRIOS	No	1.32	40	30	Super-resolution	2,719	476	12,788	-	This study
8	Titan	No	1.32	40	30	Counting	1,734	215	3,942	-	Greber et al. 2017
9	Titan	No	1.32	40	30	Counting	2,694	262	4,617	-	Greber et al. 2017
10	Titan	No	1.32	40	30	Counting	2,593	653	19,642	-	Greber et al. 2017
Σ							31,177	15,923	827,744	138,659	

1554

1555

1556 **Supplementary Table 2. Components of the TFIIH structure.**

Protein	Chain ID	Size* (aa)	Modeled residues	Sequence accession code	Alternative names	Comments
XPB	A	782	34-204, 247-730	P19447	ERCC3	-
XPD	B	760	1-760	P18074	ERCC2	4Fe4S-cluster: SF4, residue 1000.
p62	C	548	107-173, 183-323, 345-547	P32780	GTF2H1	BSD1 domain docked and refined with reference restraints; residues 233-295 built as poly-alanines and deposited as UNK.
p52	D	462	7-458	Q92759	GTF2H4	
p44	E	395	15-267, 282-387	Q13888	GTF2H2	Zn^{2+}, residues 401, 402, 403
p34	F	308	8-72, 95-292	Q13889	GTF2H3	Zn^{2+}, residues 401
p8	G	71	2-67	Q6ZYL4	GTF2H5, TTDA	-
CDK7	-	346	-	P50613	MO15	Not visualized.
Cyclin H	-	323	-	P51946	CCNH	Not visualized.
MAT1	H	309	1-210	P51948	MNAT1	N-terminal RING domain docked and refined with tight reference restraints. Zn^{2+}, residues 400, 401

1557 * According to Uniprot (http://www.uniprot.org).

1558 † Unassigned sequences were initially modeled as poly-alanine and deposited as UNK.

1559

1560

1561 **Supplementary Table 3. Data collection, map and model refinement, model**
1562 **validation.**

Data collection	**Datasets 1-6**
Microscope	Titan KRIOS
Stage type	Autoloader
Voltage (kV)	300
Detector	K2 Summit
Energy filter	GIF Quantum
Other	Volta phase plate
Pixel size (Å)	1.15
Defocus range (μm)	0.3-1.2
Electron dose (e^-/A^2)	50
Reconstruction	**EMD-XXXX**
Software	RELION 3
Particles	138,659
Box size (pixels)	256 x 256 x 256
Accuracy rotations (°)	1.4
Accuracy translations (pixels)	0.8
Map resolution (Å)	3.7
Map sharpening b-factor ($Å^2$)	-142
Coordinate refinement	
Software	PHENIX
Algorithm	REAL SPACE REFINE
Box size (Å)	294.4 x 294.4 x 294.4
Resolution cutoff (Å)	3.7
$FSC_{model\text{-}vs\text{-}map}$=0.5 (Å)	3.9
Model	**PDB-XXXX**
Number of residues	3203
Protein	3196
Ligand (Fe_4S_4, Zn^{2+})	7
B-factors overall	74.5
Protein	74.5
Ligand (Fe_4S_4)	63.4
Ligand (Zn^{2+})	133.8
R.m.s. deviations	
Bond lengths (Å)	0.009
Bond angles (°)	1.190
Validation	
Molprobity score (percentile)	2.0 (99th)
Molprobity clashscore (percentile)	6.7 (97th)
Rotamer outliers (%)	0.3
C_β deviations (%)	0
Ramachandran plot	
Favored (%)	87.8
Allowed (%)	11.9
Outliers (%)	0.3

1563
1564
1565
1566

1567 **Supplementary Discussion**

1568

1569 **Supplementary Note 1: The XPD-p44 interface.** XPD serves a dual role within
1570 TFIIH: Its helicase activity is essential for TFIIH function in NER (Kuper et al.,
1571 2014; Winkler et al., 2000), and it serves as an architectural element in
1572 transcription, enabling the proper placement of the CAK subcomplex within the
1573 Pol II PIC (Abdulrahman et al., 2013; Drapkin et al., 1996; Dubaele et al., 2003;
1574 Greber et al., 2017; Guzder et al., 1994; He et al., 2016; Murakami et al., 2015;
1575 Robinson et al., 2016; Rossignol et al., 1997; Schilbach et al., 2017; Tirode et al.,
1576 1999; Tsai et al., 2017). The XPD-p44 interaction is critical both for the
1577 enzymatic and architectural roles of XPD (Coin et al., 1998; Dubaele et al., 2003;
1578 Kim et al., 2015; Kuper et al., 2014). Therefore, disruption of the XPD-p44
1579 interface can simultaneously cause NER defects and impair transcription
1580 initiation, which leads to a TTD phenotype in human patients (Dubaele et al.,
1581 2003). Our structure provides a detailed view of this interaction interface, which
1582 encompasses the p44 loops β1-α1, β4-α5, β5-α6, and β6-α7 connecting β-strands
1583 and α-helices in the p44 VWA domain (Figure 5E, Figure 5 – figure supplement
1584 2). Mutations L174W, T175R, and D178A in the p44 β4-α5 loop have been shown
1585 to abrogate the p44-XPD interaction and to reduce the helicase activity of XPD,
1586 implicating this region in XPD activation (Kim et al., 2015; Seroz et al., 2000). Our
1587 structure suggests that the insertion of large residues (L174W, T175R) into the
1588 tightly packed p44-XPD interface (Figure 5 – figure supplement 2B) is likely to
1589 lead to steric clashes, while the D178A mutation would break a likely salt bridge
1590 with XPD R592 (Figure 5C). Strikingly, the R592P mutation in XPD, the side chain
1591 of which packs against the p44 β4-α5 loop in wild type XPD, causes TTD in
1592 human patients (Cleaver et al., 1999), underscoring the importance of this
1593 interaction.

1594

1595 In XPD, RecA2 loop residues 531-533, 563-565, 589-592, 612-616, and the
1596 helical segment 718-725 form the p44 interaction interface (Figure 5E). Using
1597 recombinant human and *Chaetomium thermophilum* proteins, it has been shown
1598 that the XPD R722W mutation impairs the interaction between p44 and XPD,
1599 thereby interfering with both the p44-dependent stimulation of the XPD ATPase

1600 and helicase activities in NER, and architectural role of p44 in transcription
1601 initiation (Kuper et al., 2014). Our structure shows that the R722W mutation
1602 disrupts a salt bridge to p44 D75, and the bulky tryptophan side chain may
1603 additionally cause steric clashes with neighboring p44 residues, explaining the
1604 deleterious effect of the mutation (Figure 5E, Figure 5 – figure supplement 2C). It
1605 has been proposed that the R616P, D673G, and G675R disease mutations, which
1606 impair the p44-XPD interaction and the XPD helicase activity (Dubaele et al.,
1607 2003), exert their deleterious effect by impairing the interaction between XPD
1608 and p62 (Luo et al., 2015). However, our structure shows that G675 is buried in
1609 the enzymatic core (Figure 5 – figure supplement 2D), where accommodation of
1610 the large arginine side chain in G675R will disrupt the structure of the protein.
1611 XPD D673 is located in a β-strand in the vicinity of the XPD-p62 interface (Figure
1612 5 – figure supplement 2D); however, no direct interactions of this residue with
1613 p62 are observed. XPD R616 is located at the p44-XPD interface, where its side
1614 chain is packed against neighboring residues and may engage in a salt bridge
1615 with p44 D204 (Figure 5 – figure supplement 2D). These interactions would be
1616 disrupted in the R616P mutant. Altogether, these observations suggest that these
1617 mutations act either via disruption of XPD structure or the XPD-p44 interface,
1618 not via p62. Nevertheless, a contribution of p62 to the stabilization of the p44-
1619 XPD interface cannot be excluded because several p62 elements are observed
1620 near the interface (Figure 5 – figure supplement 2E). As discussed in the main
1621 text, some of these interactions are dynamic (Figure 4 – figure supplement 2G-J)
1622 and unlikely to be strictly required for the stability of the p44-XPD interface.
1623
1624 **Supplementary Note 2: Mapping of XPD mutations.** In addition to our analysis
1625 of the XPD-p44 interface and the mutations located in its vicinity, we were also
1626 able to map numerous other human disease mutations onto our structure
1627 (Figure 6). Our results are in good agreement with the hypotheses derived from
1628 comparative modeling based on homologous bacterial DNA repair enzymes
1629 (Bienstock et al., 2003), archaeal XPD homologs (Fan et al., 2008; Liu et al., 2008;
1630 Wolski et al., 2008), and our previous lower-resolution TFIIH structure (Greber
1631 et al., 2017). Several XP mutations map in the regions that interact with bound
1632 DNA, as confirmed by superposing homologous DNA-bound helicase structures

1633 (Figure 6 – figure supplement 1A), or in the conserved motifs near the ATPase
1634 active site (Figure 6 – figure supplement 1B). These mutations impair XPD
1635 helicase activity (Dubaele et al., 2003; Fan et al., 2008; Liu et al., 2008), causing
1636 the NER defects that manifest in the XP disease symptoms. As explained above
1637 (Supplementary Note 1), TTD mutations tend to map to the periphery of XPD,
1638 including the XPD-p44 interface (Supplementary Note 1, Figure 5E, Figure 5 –
1639 figure supplement 2, Figure 6 – figure supplement 1C, D), the ARCH domain
1640 (Figure 6 – figure supplement 1E), or the FeS domain (Figures 5B, 6). The C259Y
1641 mutation in the ARCH domain likely impairs the proper folding of this domain
1642 due to steric hindrance introduced by the large tyrosine side chain, which in turn
1643 impairs association of the CAK subcomplex through disruption of MAT1
1644 association, as discussed previously (Greber et al., 2017; Liu et al., 2008; Wolski
1645 et al., 2008). Consistent with its observed location in our structure (Figure 5B),
1646 the R112H mutation in the FeS domain leads to destabilization of the 4FeS
1647 cluster (Rudolf et al., 2006), which in turn leads to the disruption of folding of
1648 this entire domain (Fan et al., 2008) and lower TFIIH levels overall (Botta et al.,
1649 2002). Another TTD mutation that does not localize to the periphery of XPD is
1650 the particularly interesting temperature-sensitive mutation R658C, for which
1651 patients show exacerbated symptoms, including complete hair loss, when they
1652 develop a fever (Vermeulen et al., 2001). This residue is located at the interface
1653 between the XPD RecA1 and RecA2 domains, where it forms a salt bridge across
1654 the domain interface (Figure 6B). This interface would be partially destabilized
1655 by the mutation at normal temperature and more severely disrupted at elevated
1656 temperature, leading to stronger disease symptoms.
1657
1658 We also mapped onto our structure the location of the so-called *rem* mutations in
1659 Rad3, the yeast homolog of XPD. These mutations increase the affinity of Rad3
1660 for DNA, which leads to retention of Rad3/XPD on DNA lesions, incomplete NER
1661 reactions, and subsequent DNA breakage upon arrival of a DNA replication fork
1662 (Herrera-Moyano et al., 2014; Moriel-Carretero & Aguilera, 2010). We mapped
1663 the *rem* mutations Rad3-E236G (XPD E235), Rad3-A237T (XPD A236), and
1664 Rad3-H661Y (XPD-H659Y), as well as the human XP-CS mutation XPD-G675R,
1665 which also exhibits elevated DNA affinity but reduced helicase activity in an

1666 archaeal model system (Fan et al., 2008) and DNA breakage in patient cells
1667 (Theron et al., 2005), onto our structure (Figure 6 – figure supplement 1F). XPD
1668 E235 and A236 are part of the conserved helicase motif II (signature sequence
1669 DEAH, Figure 5 – figure supplement 1C, Figure 6 – figure supplement 1F)
1670 (Fairman-Williams et al., 2010), and as such critical for nucleotide hydrolysis.
1671 Notably, the neighboring XPD D234, also part of motif II (Figure 5 – figure
1672 supplement 1C, Figure 6 – figure supplement 1C, F), is a human XP mutation
1673 (Cleaver et al., 1999). XPD H659 is located nearby, and contacts R601, which
1674 locates to the immediate vicinity of the DNA based on superposition with
1675 structures of DNA-bound helicases (Büttner et al., 2007; Cheng & Wigley, 2018)
1676 (Figure 6 – figure supplement 1F) and is affected by an XP mutation (Cleaver et
1677 al., 1999). In agreement with previous proposals, the *rem* mutations are
1678 therefore localized near regions responsible for ATP hydrolysis and DNA
1679 binding, consistent with the idea that they lead to stalling of NER complexes at
1680 DNA lesions, which may ultimately lead to incomplete NER, DNA breaks, failure
1681 to re-start transcription, and the XP-CS phenotype (Moriel-Carretero et al.,
1682 2015).
1683
1684 In summary, our structure pinpoints the locations of XPD mutations that provide
1685 insight into human disease mechanisms, and in most cases resolves the density
1686 for the side chains of the affected residues, thereby providing a structural
1687 framework for the detailed analysis of the interactions of the affected residues
1688 and the effects of these mutations.
1689
1690
1691
1692

Analysis of CX-MS data for human TFIIH

Chemical crosslinking-mass spectrometry data taken from Luo et al., Mol. Cell 59 (5): 794-806 (2015) and mapped onto the cryo-EM structure of human TFIIH.

Residues not built in in the cryo-EM structure of human TFIIH are printed red.
Crosslinking distances refer to Cα-Cα distance of crosslinked lysine residues.
The expected maxium crosslink distance for BS3-induced crosslinks is 30 Å.

Color coding for crosslinking distances:	Agreement (< 30 Å)	Borderline (30-35 Å)	Incompatible (> 35 Å)

Intramolecular crosslinks in human TFIIH subunits

Protein	Residue 1	Residue 2	Distance (Å)	Comments
p34	100	56	18.0	
p34	149	56	14.0	
p34	97	56	23.2	
p34	74	56	-	
p34	152	56	14.6	
p34	125	56	35.2	
p34	125	74	-	
MAT1	127	137	16.8	
MAT1	167	180	19.6	
MAT1	176	202	11.9	
MAT1	55	70	16.0	
MAT1	137	55	27.3	
MAT1	70	76	10.0	
MAT1	70	77	10.7	
XPD	268	274	9.7	
XPD	128	603	20.5	
XPD	692	751	28.6	
XPD	223	228	9.3	
XPD	223	69	13.0	
XPD	223	445	14.0	
XPD	223	35	16.8	
XPD	133	181	18.4	
XPD	35	751	26.8	
XPD	603	82	17.5	
XPD	228	35	10.4	
XPD	682	689	10.1	
XPD	113	603	18.6	
XPD	113	128	9.3	
XPD	113	181	11.3	
XPD	507	634	19.5	
XPD	507	682	9.8	
CDK7	32	342	-	CKD7 is not modeled in our structure.
CDK7	44	52	-	
CDK7	328	42	-	
CDK7	14	42	-	
CDK7	14	32	-	
CDK7	14	44	-	
CDK7	330	343	-	
XPB	167	222	-	Crosslink of the DRD loop insertion
XPB	167	326	16.3	
XPB	569	715	12.4	
XPB	171	311	29.2	
XPB	171	217	-	Crosslinks of the DRD loop insertion
XPB	171	222	-	that is not visible in the cryo-EM map
XPB	44	778	-	
XPB	44	68	28.1	
XPB	322	326	6.2	
XPB	157	44	13.1	
XPB	549	577	12.0	
XPB	282	463	18.0	
XPB	282	476	21.5	
XPB	577	601	11.3	
XPB	142	222	-	Crosslinks of the DRD loop insertion
XPB	142	241	-	that is not visible in the cryo-EM map
XPB	142	68	12.1	
XPB	311	379	10.0	
XPB	311	326	23.2	
XPB	217	326	-	Crosslinks of the DRD loop insertion
XPB	222	326	-	that is not visible in the cryo-EM map
XPB	222	257	-	
p62	129	504	15.3	
p62	18	38	-	Crosslinks of the N-terminal PH-
p62	104	106	-	domain of p62 and other N-terminal
p62	19	38	-	segments, which are not modeled
p62	161	38	-	in our structure.
p62	102	106	-	
p62	102	109	-	
Cyclin H	253	260	-	Cyclin H is not modeled in our
Cyclin H	274	62	-	structure.
Cyclin H	293	295	-	
Cyclin H	189	72	-	
Cyclin H	62	72	-	
Cyclin H	292	295	-	
p44	116	126	13.3	
p44	116	306	20.1	
p44	116	157	15.6	
p44	23	40	18.2	
p44	126	23	55.5	
p44	126	306	16.9	
p44	126	133	10.4	
p44	126	268	28.6	
p44	126	297	20.4	
p52	76	81	10.1	
p52	452	459	-	
p52	452	456	6.7	
p52	378	53	31.8	
p52	127	53	24.6	
p8	2	31	24.5	
p8	6	31	17.0	

Intermolecular crosslinks in human TFIIH subunits

Protein 1	Residue 1	Protein 2	Residue 2	Distance (Å)	Comments
p34	149	p52	378	15.3	
p34	152	p52	378	10.2	
p34	97	p52	127	8.7	
XPB	379	XPD	682	29.7	
XPB	222	XPD	682	-	
XPB	326	XPD	682	18.4	
XPB	171	XPD	682	19.6	
XPB	171	XPD	507	19.1	
p62	378	p34	125	25.7	
p62	38	p34	125	-	
p62	38	XPB	549	-	
p62	353	p44	126	50.0	p62-p44 crosslinks were discarded
p62	38	p44	126	-	in modeling due to high incidence
p62	252	p44	31	73.1	of distance violations and excellent
p62	161	p44	116	22.3	agreement of p62 model with
p62	161	p44	126	34.0	p62-XPD crosslinks.
p62	350	XPD	82	10.2	
p62	350	XPD	113	17.0	
p62	365	XPD	96	16.9	
p62	353	XPD	603	19.6	
p62	353	XPD	113	20.8	
p62	353	XPD	82	9.4	
p62	275	XPD	603	13.6	
p62	293	XPD	603	23.0	
p62	293	XPD	113	32.1	
p62	296	XPD	603	25.7	
Cyclin H	239	MAT1	55	-	Cyclin H is not modeled.
MAT1	121	XPB	44	116.7	
MAT1	180	XPB	171	17.7	
MAT1	202	XPB	142	37.5	
MAT1	176	XPB	171	19.3	
MAT1	167	XPB	217	-	Crosslinks of the DRD loop insertion
MAT1	167	XPB	222	-	that is not visible in the cryo-EM map
MAT1	167	XPB	257	19.1	
MAT1	167	XPD	689	26.9	
MAT1	167	XPD	634	19.7	
p44	40	p34	149	21.0	
p44	126	p34	149	34.1	
p44	42	p34	149	22.2	
p44	229	p34	149	23.0	
p44	229	p34	152	26.7	
p44	23	XPB	142	7.7	
p44	31	XPB	142	8.7	
p44	23	p52	378	32.7	
p44	40	p52	378	23.2	
p44	268	p52	77	30.0	
p44	77	p52	378	20.8	
p52	438	XPB	526	33.9	
p52	438	XPB	706	20.4	
p52	378	XPB	526	51.6	
p52	378	XPB	241	-	
p52	378	XPB	257	63.0	
p52	140	XPD	29	92.4	Likely false positives given the reliable
p52	277	XPD	101	116.0	assignment of p52 and XPD.
p52	53	p8	31	59.3	
p52	452	p8	2	9.8	
p52	452	p8	6	12.5	
p52	77	p8	71		
p52	456	p8	2	11.8	
p52	456	p8	6	18.5	
CDK7	52	Cyclin H	293	-	CDK7 and Cyclin H are not modeled
CDK7	293	XPD	634	-	CDK7 is not modeled.
p8	71	XPB	767	-	Crosslinks of p8 with the XPB RecA2
p8	71	XPB	526	-	domain are compatible with the
p8	71	XPB	59	-	architecture of TFIIH overall.
p8	71	XPB	476	-	
p8	6	XPB	167	88.0	